

Serena R. Scholz

**Use of high-resolution oxygen isotope sclerochronology of turritellid gastropods to reconstruct seasonal-scale precipitation regimes**

Ch1: Isotope sclerochronology indicates enhanced seasonal precipitation in northern South America (Colombia) during the Mid Miocene Climatic Optimum

Ch2: A modern calibration for the reconstruction of seasonal precipitation patterns from isotope sclerochronology of coastal turritellid gastropods

submitted in partial fulfillment of the requirements for the degree of  
**Master of Science in Earth and Environmental Sciences**  
Department of Earth and Environmental Sciences  
The University of Michigan

Accepted by:

_____	Sierra V. Petersen	04/28/20
Signature	Name	Date
_____	Julia Cole	04/29/20
Signature	Name	Date
_____		
Department Chair Signature	Name	Date

I hereby grant the University of Michigan, its heirs and assigns, the non-exclusive right to reproduce and distribute single copies of my thesis, in whole or in part, in any format. I represent and warrant to the University of Michigan that the thesis is an original work, does not infringe or violate any rights of others, and that I make these grants as the sole owner of the rights to my thesis. I understand that I will not receive royalties for any reproduction of this thesis.

- Permission granted.
- Permission granted to copy after: Dec 31st, 2021
- Permission declined.

*Serena R. Scholz*

Author Signature



# **Isotope sclerochronology indicates enhanced seasonal precipitation in northern South America (Colombia) during the Mid-Miocene Climatic Optimum**

## **Abstract**

During the Mid-Miocene Climatic Optimum (MMCO, 14.7-17.3 Ma), global temperatures were warmer than present, and similar to predicted temperatures for the coming century. Limited paleoclimate data exists from the tropics during this period, despite its potential as an analog for future climate conditions. This study presents new subannual stable isotope data ( $\delta^{18}\text{O}$  and  $\delta^{13}\text{C}$ ) from a large population of Miocene *Turritella* gastropods from the Jimol and Castilletes formations of the Guajira peninsula, Colombia. Turritellids are aragonitic marine mollusks that live in shallow coastal waters, and their rapid growth rates allow for high-resolution subannual records. We compare these fossils to modern *Turritella* gastropods from multiple tropical localities to reconstruct subannual climate conditions. The seasonal range in  $\delta^{18}\text{O}$  in the modern shells correlates with the seasonal variance of local precipitation, once temperature seasonality is accounted for. The Miocene fossils show larger (sometimes  $>2\%$ ) seasonal variation in  $\delta^{18}\text{O}$  than modern *Turritella* from the same location, suggesting increased seasonality of precipitation in Miocene northern Colombia relative to today. We propose that this increased seasonality of precipitation was due to a more northerly position of the ITCZ during the Mid-Miocene. The resulting wet Miocene paleoenvironment is in stark contrast to semi-arid conditions on the Guajira Peninsula today, indicating that this area of tropical South America has undergone a drastic environmental change since the Miocene.

## **Introduction**

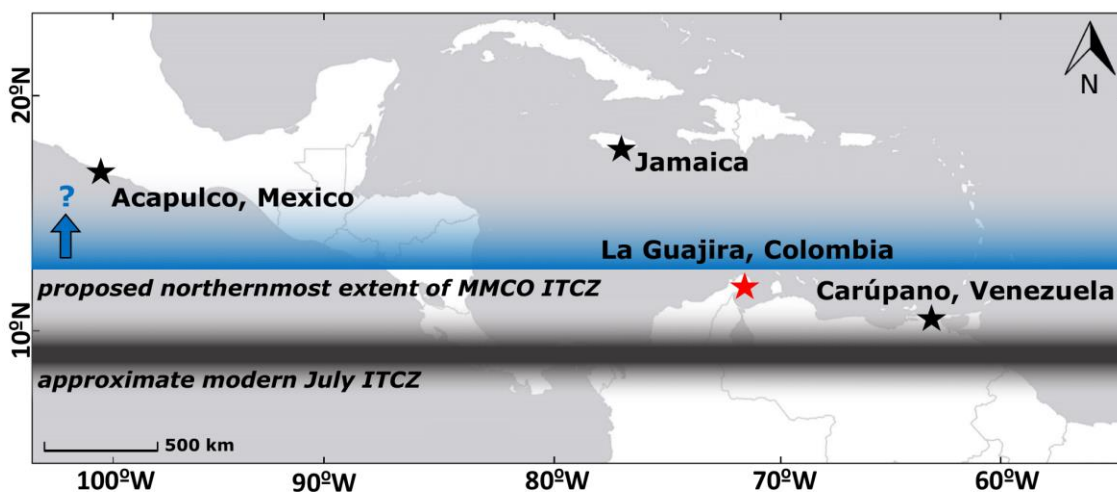
The Mid-Miocene Climatic Optimum (MMCO, 14.7-17.3 Ma) was a brief return to warmer conditions embedded within the cooling trend of the Cenozoic (Zachos et al., 2001, Cramer et al., 2009). Continental and ocean temperatures were warmer than the Neogene average, potentially driven by atmospheric  $\text{CO}_2$  concentrations of 400 ppm or higher (Greenop et al., 2013; Londoño et al., 2018), making the period a potential analog for future climate. However, most studies to date have been constrained to higher latitudes (Goldner et al., 2014), so there is little known about tropical climate during the MMCO. Tropical paleotemperature estimates are limited to a handful of  $\delta^{18}\text{O}$  analyses of planktonic foraminifera (Savin et al., 1981, Woodruff et al., 1991) and a single alkenone-based temperature record from the Pacific (Rousselle et al., 2013).  $\delta^{18}\text{O}$  measurements of freshwater bivalves from Peru found that MMCO precipitation intensity was comparable to modern (Kaandorp et al., 2005), but these few sites are insufficient to infer larger-scale temperature and precipitation patterns.

A new set of geological outcrops has recently been described on the Guajira Peninsula of Colombia ( $12^\circ\text{N}$ , paleolatitude  $8^\circ\text{N}$ ). This continuous early Neogene section has a robust strontium-isotope-based chronostratigraphy (Hendy et al., 2015) and contains well-preserved plant, vertebrate, and invertebrate fossils. The Jimol and Castilletes Formations both date to the mid-Miocene, and include abundant fossil turritellids (Moreno et al., 2015). Turritellids are

aragonitic marine mollusks with rapid growth rates, making them a good target for subannual paleoclimate reconstructions (Jones and Allmon, 1995; Tripathi et al., 2009; Anderson et al., 2017). Their shallow coastal habitat (often <5m) means that the shells are likely influenced by both ocean temperature changes and by changes in water isotopic composition from continental runoff (Allmon, 2011). We apply high-resolution stable isotope sampling techniques to turritellid shells to reconstruct subannual climate and hydrological conditions on the Guajira Peninsula during the MMCO.

## Methods

Twenty-five fossil turritellid gastropods representing seven species were collected from the Jimol and Castilletes Formations on the Guajira Peninsula (Figure 1, Figure DR2), from ten stratigraphic levels dating from 14.7-17.3 Ma (Figure DR3). Eight modern turritellids of three species were either collected on the Guajira Peninsula (locality 290628, Figure DR2), or borrowed from the University of Michigan Zoology Collections (Venezuela, Jamaica, and Mexico, Figure 1).



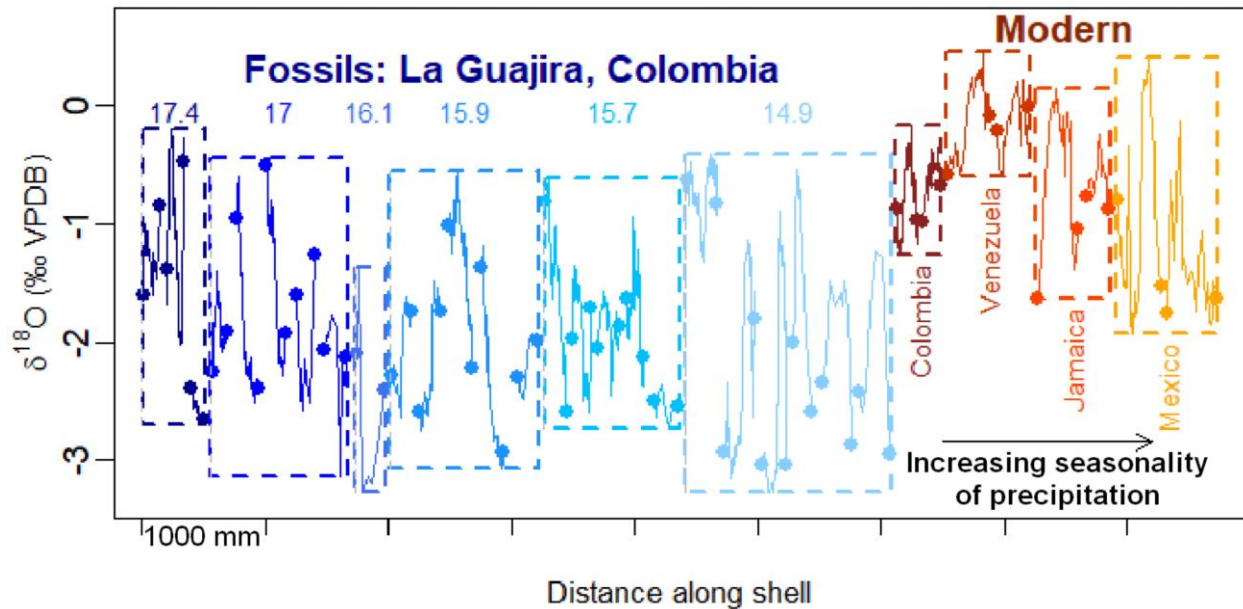
**Figure 1: Map of collection locations and proposed changes in ITCZ position.** Modern shells were collected at all 4 locations shown. Miocene shells were collected from the Guajira Peninsula, Colombia. Proposed Miocene ITCZ shown in blue is a southward limit given our sampling location.

Shells were analyzed using Raman spectroscopy, SEM and XRD, all of which showed excellent preservation. Subannual variations in shell carbonate  $\delta^{18}\text{O}$  can be resolved without microscopic sampling due to rapid growth rates, and typically show a sinusoidal pattern of highs and lows along the growth axis. All shells were drilled at a subannual scale along the spiral growth direction, and powders were analyzed for  $\delta^{18}\text{O}$  and  $\delta^{13}\text{C}$ . All  $\delta^{13}\text{C}$  and  $\delta^{18}\text{O}$  values are presented relative to VPDB, and are available in Table DR2. See supplementary material for more detail on sampling, isotopic analysis, and preservation assessment.

## Results

$\delta^{18}\text{O}$  values in modern shells varied from -1.9 to 0.5‰, with seasonal ranges of 0.6-2.3‰ within a single shell, varying by location (Figure 2).  $\delta^{18}\text{O}$  values for all Miocene shells were lower on average than the modern shells, between -3.3‰ and -0.2‰. Within a given fossil shell, the total range in  $\delta^{18}\text{O}$  (max. to min.) varied from 0.3‰ to 2.4‰. The maximum range in  $\delta^{18}\text{O}$  seen in a single fossil shell (2.4‰) was more than twice as large as the maximum range seen in modern Guajira Peninsula shells (1.1‰), and was similar to the  $\delta^{18}\text{O}$  range recorded by a modern turritellid from Mexico (2.3‰). Within the fossil shells, there is no correlation between  $\delta^{18}\text{O}$  range and environmental parameters such as estimated water depth, paleosalinity, and stratigraphic height (Figure DR7), or between size of shell, species or individual lifespan (Figure DR8), suggesting all shells accurately capture near-surface conditions without environmental or ecological biases.

$\delta^{13}\text{C}$  values for all fossil shells were between -1.8‰ and 3.8‰, with 90% between 1.5‰ and 3.8‰. Modern shells showed similar  $\delta^{13}\text{C}$  values ranging from 1.3 to 3.5‰. Variations in  $\delta^{13}\text{C}$  in both modern and fossil shells did not show coherent subannual patterns like those seen in  $\delta^{18}\text{O}$ , and there was no correlation between range in  $\delta^{13}\text{C}$  and range in  $\delta^{18}\text{O}$ .



**Figure 2:**  $\delta^{18}\text{O}$  sclerochronologies of all shells. Fossil shells are arranged by horizon age. Other than Guajira Peninsula, modern shells are arranged by increasing precipitation variance. Boxes show range in  $\delta^{18}\text{O}$  for each fossil horizon or modern location.  $\delta^{18}\text{O}$  is plotted against the accumulated distance in the spiral growth direction.

## Discussion:

### *Link between $\delta^{18}\text{O}$ range and seasonality of precipitation in modern shells*

Turritellids live in shallow coastal waters, often less than 5m deep (Allmon, 2011). The  $\delta^{18}\text{O}$  recorded in their shells is controlled by both sea surface temperatures (SST) and the oxygen isotopic composition of seawater ( $\delta^{18}\text{O}_{\text{sw}}$ ) at time of shell formation. Using observed (instrumental) changes in SST at each modern site, the expected variation in carbonate  $\delta^{18}\text{O}$  caused by seasonal SST change alone can be calculated ( $\Delta\text{SST}$  Equivalent in  $\Delta\delta^{18}\text{O}_{\text{carb}}$ , Table 1). If this value is subtracted from the full  $\delta^{18}\text{O}$  range, the remaining variability in  $\delta^{18}\text{O}$  must reflect

seasonal changes in  $\delta^{18}\text{O}_{\text{sw}}$  (Apparent  $\Delta\delta^{18}\text{O}_{\text{sw}}$ , Table 1), assuming the two variables are varying constructively and in-phase. This assumption is reasonable to make in this case, as the four modern sites receive maximum precipitation in the summer/fall, not in the winter, where destructive interference with the temperature signal would be highest.

Shallow coastal water temperatures and  $\delta^{18}\text{O}_{\text{sw}}$  values can be influenced by both continental freshwater input and seasonal upwelling. Seasonal upwelling brings colder waters up from depth, cooling coastal SSTs. None of our modern sites are in previously identified areas of strong upwelling (Rueda-Roa et al., 2018; Portela et al., 2016), and the local instrumental SST values used in our analysis should incorporate any seasonal temperature changes resulting from upwelling. At shallow depths, upwelling could cause a minor reduction in shallow water temperature, but it would likely have a negligible effect on the  $\delta^{18}\text{O}_{\text{sw}}$  given that the gradient of  $\delta^{18}\text{O}_{\text{sw}}$  with depth is very gradual; profiles of  $\delta^{18}\text{O}_{\text{sw}}$  in coastal Indian ocean environments show variations of  $<0.3\text{‰}$  in the top 160m (Candelier et al., 2013).

TABLE 1. ISOTOPIC AND CLIMATE DATA FROM ALL SITES

Location	Annual SST Variation ( $^{\circ}\text{C}$ )*	Annual $\Delta\text{SST}$ ( $^{\circ}\text{C}$ )	$\Delta\text{SST}$ Equivalent in $\Delta\delta^{18}\text{O}_{\text{carb}}$ ( $\text{‰}$ ) <sup>†</sup>	Maximum Observed $\Delta\delta^{18}\text{O}_{\text{carb}}$ ( $\text{‰}$ )	Apparent $\Delta\delta^{18}\text{O}_{\text{sw}}$ ( $\text{‰}$ ) <sup>§</sup>	Mean Annual Precipitation (mm) <sup>#</sup>	Seasonal Variance in Precipitation (mm) <sup>**</sup>
<u>Modern sites</u>							
Guajira, CO	24.9-27.9	3.0	0.43	1.09	0.45	892	186
Carupano, VE	23.4-26.8	3.4	0.72	1.04	0.32	1282	147
Jamaica	26.5-29.5	3.0	0.64	1.78	1.14	2153	246
Acapulco, MX	25.6-30.5	4.9	1.04	2.34	1.30	1215	288
<u>Miocene site</u>							
Guajira, CO	unknown	3.0 <sup>††</sup>	0.43	2.39	1.96	unknown	unknown

\*See Table DR4 for SST data sources and comparison between local instrumental records and regional satellite-derived SSTs.

<sup>†</sup>Calculated using the mollusk equation of Grossman and Ku (1986), assuming an invariant  $\delta^{18}\text{O}_{\text{seawater}}$  value and the instrumental seasonal change shown by  $\Delta\text{SST}$ .

<sup>§</sup>Calculated as the maximum observed  $\Delta\delta^{18}\text{O}_{\text{carbonate}}$  (seasonal min. to max.  $\delta^{18}\text{O}_{\text{carb}}$  of a shell), minus the  $\Delta\text{SST}$  Equivalent in  $\Delta\delta^{18}\text{O}_{\text{carb}}$

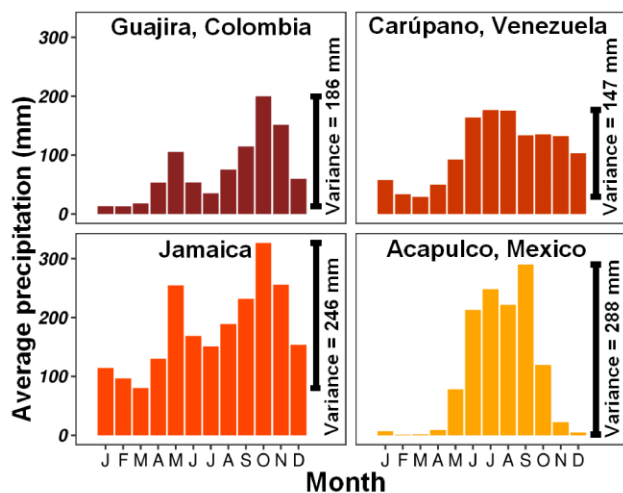
<sup>#</sup>Derived from the CRU 3.25 Global Precipitation dataset, calculated by averaging over the relevant region (Figure DR1) and summing monthly means over the period 1930-2012.

<sup>\*\*</sup>Calculated as the difference between the rainiest and driest monthly means.

<sup>††</sup>Assumed to be equivalent to modern Guajira.

In contrast to upwelling, input of freshwater to shallow coastal environments can dramatically change local  $\delta^{18}\text{O}_{\text{sw}}$ . Freshwater input integrates regional and local precipitation patterns, and is usually depleted by at least 4-6‰ relative to seawater. Even a modest freshwater input (25%) could reduce  $\delta^{18}\text{O}_{\text{sw}}$  by 1‰, which would translate directly into an equivalent change in  $\delta^{18}\text{O}_{\text{carb}}$ . The effect of increased freshwater input can also be seasonally variable (Figure 3). Locations with highest seasonal precipitation variance (difference between rainiest and driest monthly mean precipitation) should have the greatest variation in freshwater delivery throughout the year and therefore the greatest seasonal variation in coastal  $\delta^{18}\text{O}_{\text{sw}}$ , as any isotopic anomalies in  $\delta^{18}\text{O}_{\text{sw}}$  would be mixed away by ocean currents relatively quickly.

We find that the apparent seasonal variability in  $\delta^{18}\text{O}_{\text{sw}}$  is higher at sites with higher seasonal variance in regional precipitation (Table 1, Figure DR12). For example, one sample from Mexico has an apparent  $\delta^{18}\text{O}_{\text{sw}}$  variation  $\sim 2$  times higher and a seasonal precipitation variance  $\sim 50\%$  higher than the modern Guajira Peninsula shells. In contrast, there does not seem to be a relationship between mean annual precipitation (MAP) and apparent  $\delta^{18}\text{O}_{\text{sw}}$  variation. We suggest that the locations with a higher MAP may have lower coastal  $\delta^{18}\text{O}_{\text{sw}}$  values on average year-round, but this does not affect the seasonal variation in  $\delta^{18}\text{O}_{\text{sw}}$ .



**Figure 3: Monthly precipitation at all modern locations.** Monthly mean precipitation data was calculated from the CRU 3.25 Global Precipitation dataset. Seasonal variance (black bar) was calculated as the difference between the rainiest and driest monthly means.

### Seasonal variability in Miocene climate and environment

The seasonal range in  $\delta^{18}\text{O}$  observed in the Miocene fossil shells is consistently larger than that in modern shells from the Guajira Peninsula (maximum of 2.4‰ for fossils vs. 1.1‰ for modern). Seasonal ranges of  $>1.3\text{‰}$  are present in 77% of fossil shells with lifespans of one full year or more. The average range among all fossil shells (including those that lived  $<1$  year) is 1.4‰, compared to 0.8‰ for the modern samples.

Assuming a temperature seasonality similar to the modern Guajira Peninsula ( $3.0^\circ\text{C}$ ), we calculate an apparent  $\Delta\delta^{18}\text{O}_{\text{sw}}$  of 2.0‰ (Table 1). This apparent  $\Delta\delta^{18}\text{O}_{\text{sw}}$  is much larger than seen in the modern shells from the same site (0.5‰), as well as all other modern sites. If the relationship between seasonal variance of precipitation and apparent  $\Delta\delta^{18}\text{O}_{\text{sw}}$  seen across the four modern locations holds true, then the Miocene Guajira Peninsula must have experienced

significantly more seasonality of precipitation than it does today, potentially similar to the modern seasonal variance of 288mm seen in Acapulco, Mexico. If temperatures are assumed to be warmer during the Miocene, as some evidence indicates (Londoño et al., 2018), the seasonal SST range may have been reduced relative to today, in which case the apparent  $\Delta\delta^{18}\text{O}_{\text{sw}}$  and, by proxy, the influence of seasonal freshwater delivery, may have been even higher.

Faunal and sedimentological evidence from the Guajira Peninsula indicate that Miocene environment was rainier than present, with a significant freshwater influx. Isotopic analyses of bioapatite from fossil elasmobranch teeth point to a marine environment with a strong seasonal freshwater influence (Carrillo-Briceño et al., 2019), supporting our interpretation of increased seasonal precipitation variance. Fauna from the Castilletes Formation suggest an overall wetter Miocene environment on the Peninsula, including year-round rivers, swamps and lakes (Moreno et al., 2015; Carrillo et al., 2018). Evidence from the overlying Ware Formation indicates that these wet conditions persisted until at least the Pliocene. A provenance analysis from Pliocene-age sediments found that freshwater entering coastal waters off the Peninsula was sourced locally in the Guajira mountains (Perez-Consuegra et al., 2018), which could reasonably also be the case during the MMCO. One potential source of freshwater delivery to the Guajira coast could have been the proto-Orinoco river, which is thought to have drained into the Gulf of Venezuela during the early Miocene (Diaz de Gamero, 1996) and would have integrated regional precipitation patterns.

Combined with our above interpretation of a higher seasonality of precipitation during the MMCO, this interpretation of a seasonally rainy climate with year-round bodies of water differs dramatically from the modern Guajira Peninsula, which has an arid climate, mean annual precipitation of <500mm, and >10 months of dry season according to local stations close to the sampling site (Poveda et al., 2006).

### ***Past movement of the ITCZ***

To sustain the wet-loving fauna and produce the inferred seasonal  $\delta^{18}\text{O}_{\text{sw}}$  variations, increased seasonal precipitation in the region is needed. One way in which precipitation could be seasonally enhanced is through the northward migration of the intertropical convergence zone (ITCZ), which has dominant control over the magnitude of riverine discharge across many drainage basins in northern South America (Hastenrath, 1990). Presently, the ITCZ only reaches the Guajira Peninsula at its northernmost position during the boreal summer, resulting in little rainfall in the region (Figure 1, Poveda et al., 2006). A slight northward migration of the ITCZ would place the Guajira Peninsula in a higher rainfall belt and seasonally enhance precipitation in the boreal summer. Miocene bivalves at 3°S in Peru show seasonal  $\delta^{18}\text{O}$  variations consistent with modern rainfall patterns, indicating that the ITCZ likely still passed south of 3°S at its southernmost extent, as it does today (Kaandorp et al., 2005).

Models suggest that the position of the ITCZ shifts meridionally away from the hemisphere with increased ice cover (Chiang et al., 2005), and paleorecords indicate north–south shifts in the mean position of the ITCZ towards the warmer hemisphere across Pleistocene and Holocene events (McGee et al., 2014) and the Oligocene-Miocene boundary (Hyeong et al., 2014). Significant northern hemisphere glaciation is thought to have begun during the late Pliocene and early Pleistocene, around 3.2-2.7 Ma (Bartoli et al., 2005). This glaciation would



have shifted the position of the ITCZ southward, coincident with the rough timing of increased aridity on the Guajira Peninsula, which occurred after the deposition of the Pliocene Ware formation (3.5-2.8 Ma; Moreno et al., 2015). Lower topography during the Miocene could also have played a role in enhancing precipitation (Henrot et al., 2010), but sensitivity modeling of South America indicates that precipitation should be lower than today in northern Guajira when the Andes have a lower elevation (Sepulchre et al., 2010). Additional studies are needed to constrain the timing and cause of this climatic change more precisely, but it is clear that wet conditions, significantly different from today, persisted on the Guajira Peninsula from the Miocene to the Pliocene.

### **Conclusion:**

When considering the effects of future global warming, changes in precipitation are more difficult to predict than changes in temperature, with many models disagreeing on whether future rainfall will increase or decrease (Trenberth 2011). This divergence in model prediction is stronger within tropical latitudes (Joetzer et al., 2013), where water availability is of critical importance and is the key factor determining biome extent (Jaramillo and Cardenas, 2013). Our isotopic data combined with faunal evidence indicate a wetter environment in northern South American during the Miocene, with increased seasonal variance of precipitation. A more northerly position of the ITCZ during the MMCO (potentially sustained until the Pliocene) could produce the inferred seasonally enhanced precipitation on the Guajira Peninsula. This study provides new data from a region that has been previously understudied in terms of paleoclimate reconstructions, but further research from other areas is still needed in order to better constrain precipitation patterns in the tropics and movement of the ITCZ during the MMCO.

### **Acknowledgements:**

We thank many who helped with field work, as well as L. Wingate, K. Lohmann, C. Nims, J. Johnson and O. Neill for technical support. Field work was sponsored by STRI, Universidad del Norte, and University of Zurich. SRS was supported by U of M UROP. SVP was supported by NSF-OCE-PRF #1420902. JE was partially funded by Colciencias Grant #121566044585. CJ was funded by STRI, the Anders Foundation, 1923 Fund, G.D. and J.W. Johnson, and NSF EAR #0957679.

### **References Cited**

- Allmon, W.D., 2011, Natural History of Turritelline Gastropods (Cerithioidea: Turritellidae): A Status Report: *Malacologia*, v. 54, p. 159–202, doi:[10.4002/040.054.0107](https://doi.org/10.4002/040.054.0107).
- Anderson, B.M., Hendy, A., Johnson, E.H., Allmon, W.D., 2017, Paleocology and paleoenvironmental implications of turritelline gastropod-dominated assemblages from the Gatun Formation (Upper Miocene) of Panama. *Palaeogeography, Palaeoclimatology, Palaeoecology*, v. 470, p. 132-146, doi: [10.1016/j.palaeo.2017.01.026](https://doi.org/10.1016/j.palaeo.2017.01.026)
- Bartoli, G., Sarnthein, M., Weinelt, M., Erlenkeuser, H., Garbe-Schönberg, D., and Lea, D.W., 2005, Final closure of Panama and the onset of northern hemisphere glaciation: *Earth and Planetary Science Letters*, v. 237, p. 33–44, doi:[10.1016/j.epsl.2005.06.020](https://doi.org/10.1016/j.epsl.2005.06.020).



- Candelier, Y., Minoletti, F., Probert, I., and Hermoso, M., 2013, Temperature dependence of oxygen isotope fractionation in coccolith calcite: A culture and core top calibration of the genus *Calcidiscus*: *Geochimica et Cosmochimica Acta*, v. 100, p. 264–281, doi:[10.1016/j.gca.2012.09.040](https://doi.org/10.1016/j.gca.2012.09.040).
- Carrillo, J.D., Amson, E., Jaramillo, C., Sánchez, R., Quiroz, L., Cuartas, C., Rincón, A.F., and Sánchez-Villagra, M.R., 2018, The Neogene Record of Northern South American Native Ungulates: *Smithsonian Contributions to Paleobiology*, p. iv–67, doi:[10.5479/si.1943-6688.101](https://doi.org/10.5479/si.1943-6688.101).
- Carrillo-Briceño, J.D., Luz, Z., Hendy, A., Kocsis, L., Aguilera, O., and Vennemann, T., 2019, Neogene Caribbean elasmobranchs: diversity, paleoecology and paleoenvironmental significance of the Cocinetas Basin assemblage (Guajira Peninsula, Colombia): *Biogeosciences*, v. 16, p. 33–56, doi:[10.5194/bg-16-33-2019](https://doi.org/10.5194/bg-16-33-2019).
- Chiang, J.C.H., and Bitz, C.M., 2005, Influence of high latitude ice cover on the marine Intertropical Convergence Zone: *Climate Dynamics*, v. 25, p. 477–496, doi:[10.1007/s00382-005-0040-5](https://doi.org/10.1007/s00382-005-0040-5).
- Cramer, B.S., Toggweiler, J.R., Wright, J.D., Katz, M.E., and Miller, K.G., 2009, Ocean overturning since the Late Cretaceous: Inferences from a new benthic foraminiferal isotope compilation: *Benthic Isotope Compilation: Paleoceanography*, v. 24, doi:[10.1029/2008PA001683](https://doi.org/10.1029/2008PA001683).
- Díaz de Gamero, M.L., 1996, The changing course of the Orinoco River during the Neogene: a review: *Palaeogeography, Palaeoclimatology, Palaeoecology*, v. 123, p. 385–402, doi:[10.1016/0031-0182\(96\)00115-0](https://doi.org/10.1016/0031-0182(96)00115-0).
- Goldner, A., Herold, N., and Huber, M., 2014, The challenge of simulating the warmth of the mid-Miocene climatic optimum in CESM1: *Climate of the Past*, v. 10, p. 523–536, doi:[10.5194/cp-10-523-2014](https://doi.org/10.5194/cp-10-523-2014).
- Greenop, R., Foster, G.L., Wilson, P.A., and Lear, C.H., 2014, Middle Miocene climate instability associated with high-amplitude CO<sub>2</sub> variability: Large variability in Middle Miocene CO<sub>2</sub>: *Paleoceanography*, v. 29, p. 845–853, doi:[10.1002/2014PA002653](https://doi.org/10.1002/2014PA002653).
- Grossman, E. L., and Ku, T. L., 1986, Oxygen and carbon isotope fractionation in biogenic aragonite: temperature effects: *Chemical Geology: Isotope Geoscience Section*, v. 59, p. 59-74.
- Hastenrath, S., 1990, Diagnostics and Prediction of Anomalous River Discharge in Northern South America: *Journal of Climate*, v. 3, p. 1080–1096, doi:[10.1175/1520-0442\(1990\)003<1080:DAPOAR>2.0.CO;2](https://doi.org/10.1175/1520-0442(1990)003<1080:DAPOAR>2.0.CO;2).
- Hendy, A.J.W., Jones, D.S., Moreno, F., Zapata, V., and Jaramillo, C., 2015, Neogene molluscs, shallow marine paleoenvironments, and chronostratigraphy of the Guajira Peninsula, Colombia: *Swiss Journal of Palaeontology*, v. 134, p. 45–75, doi:[10.1007/s13358-015-0074-1](https://doi.org/10.1007/s13358-015-0074-1).
- Henrot, A.-J., François, L., Favre, E., Butzin, M., Ouberdous, M., and Munhoven, G., 2010, Effects of CO<sub>2</sub>, continental distribution, topography and vegetation changes on the climate at the Middle Miocene: a model study: *Climate of the Past*, v. 6, p. 675–694, doi:[10.5194/cp-6-675-2010](https://doi.org/10.5194/cp-6-675-2010).

- Hyeong, K., Lee, J., Seo, I., Lee, M.J., Yoo, C.M., and Khim, B.-K., 2014, Southward shift of the Intertropical Convergence Zone due to Northern Hemisphere cooling at the Oligocene-Miocene boundary: *Geology*, v. 42, p. 667–670, doi:[10.1130/G35664.1](https://doi.org/10.1130/G35664.1).
- Jaramillo, C., and Cárdenas, A., 2013, Global Warming and Neotropical Rainforests: A Historical Perspective: *Annual Review of Earth and Planetary Sciences*, v. 41, p. 741–766, doi:[10.1146/annurev-earth-042711-105403](https://doi.org/10.1146/annurev-earth-042711-105403).
- Joetzjer, E., Douville, H., Delire, C., and Ciais, P., 2013, Present-day and future Amazonian precipitation in global climate models: CMIP5 versus CMIP3: *Climate Dynamics*, v. 41, p. 2921–2936.
- Jones, D.S., and Allmon, W.D., 1995, Records of upwelling, seasonality and growth in stable-isotope profiles of Pliocene mollusk shells from Florida: *Lethaia*, v. 28, p. 61–74, doi:[10.1111/j.1502-3931.1995.tb01593.x](https://doi.org/10.1111/j.1502-3931.1995.tb01593.x).
- Kaandorp, R.J.G., Vonhof, H.B., Wesselingh, F.P., Pittman, L.R., Kroon, D., and van Hinte, J.E., 2005, Seasonal Amazonian rainfall variation in the Miocene Climate Optimum: *Palaeogeography, Palaeoclimatology, Palaeoecology*, v. 221, p. 1–6, doi:[10.1016/j.palaeo.2004.12.024](https://doi.org/10.1016/j.palaeo.2004.12.024).
- Londoño, L., Royer, D.L., Jaramillo, C., Escobar, J., Foster, D.A., Cárdenas-Rozo, A.L., and Wood, A., 2018, Early Miocene CO<sub>2</sub> estimates from a Neotropical fossil leaf assemblage exceed 400 ppm: *American Journal of Botany* v. 105, p. 1929–1937. doi:[10.1002/ajb2.1187](https://doi.org/10.1002/ajb2.1187)
- McGee, D., Donohoe, A., Marshall, J., and Ferreira, D., 2014, Changes in ITCZ location and cross-equatorial heat transport at the Last Glacial Maximum, Heinrich Stadial 1, and the mid-Holocene: *Earth and Planetary Science Letters*, v. 390, p. 69–79, doi:[10.1016/j.epsl.2013.12.043](https://doi.org/10.1016/j.epsl.2013.12.043).
- Poveda, G., Waylen, P.R., Pulwarty, R.S., 2006, Annual and inter-annual variability of the present climate in northern South America and southern Mesoamerica: *Palaeogeography, Palaeoclimatology, Palaeoecology*, v. 234, p. 3–27, doi: [10.1016/j.palaeo.2005.10.031](https://doi.org/10.1016/j.palaeo.2005.10.031).
- Moreno, F. et al., 2015, Revised stratigraphy of Neogene strata in the Cocinetas Basin, La Guajira, Colombia: *Swiss Journal of Palaeontology*, v. 134, p. 5–43, doi:[10.1007/s13358-015-0071-4](https://doi.org/10.1007/s13358-015-0071-4).
- Pérez-Consuegra, N., Parra, M., Jaramillo, C., Silvestro, D., Echeverri, S., Montes, C., Jaramillo, J.M., and Escobar, J., 2018, Provenance analysis of the Pliocene Ware Formation in the Guajira Peninsula, northern Colombia: Paleodrainage implications: *Journal of South American Earth Sciences*, v. 81, p. 66–77, doi:[10.1016/j.jsames.2017.11.002](https://doi.org/10.1016/j.jsames.2017.11.002).
- Portela, E., Beier, E., Barton, E.D., Castro, R., Godínez, V., Palacios-Hernández, E., Fiedler, P.C., Sánchez-Velasco, L., and Trasviña, A., 2016, Water Masses and Circulation in the Tropical Pacific off Central Mexico and Surrounding Areas: *Journal of Physical Oceanography*, v. 46, p. 3069–3081, doi:[10.1175/JPO-D-16-0068.1](https://doi.org/10.1175/JPO-D-16-0068.1).
- Rousselle, G., Beltran, C., Sicre, M.-A., Raffi, I., and De Rafélis, M., 2013, Changes in sea-surface conditions in the Equatorial Pacific during the middle Miocene–Pliocene as inferred from coccolith geochemistry: *Earth and Planetary Science Letters*, v. 361, p. 412–421, doi:[10.1016/j.epsl.2012.11.003](https://doi.org/10.1016/j.epsl.2012.11.003).

- Rueda-Roa, D., Ezer, T., and Muller-Karger, F., 2018, Description and Mechanisms of the Mid-Year Upwelling in the Southern Caribbean Sea from Remote Sensing and Local Data: *Journal of Marine Science and Engineering*, v. 6, p. 36, doi:10.3390/jmse6020036.
- Savin, S.M., Douglas, R.G., Keller, G., Killingley, J.S., Shaughnessy, L., Sommer, M.A., Vincent, E., and Woodruff, F., 1981, Miocene benthic foraminiferal isotope records: A synthesis: *Marine Micropaleontology*, v. 6, p. 423–450, doi:[10.1016/0377-8398\(81\)90031-1](https://doi.org/10.1016/0377-8398(81)90031-1).
- Sepulchre, P., Sloan, L. C., and Fluteau, F., 2010, Modelling the response of Amazonian climate to the uplift of the Andean mountain range, in Hoorn, M. C., and Wesselingh, F. P., eds., *Amazonia, Landscape and Species Evolution: A Look into the Past*: Oxford, Wiley-Blackwell Publishing, p. 211-222.
- Trenberth, K., 2011, Changes in precipitation with climate change: *Climate Research*, v. 47, p. 123–138, doi:[10.3354/cr00953](https://doi.org/10.3354/cr00953).
- Tripati, A.K., Allmon, W.D., and Sampson, D.E., 2009, Possible evidence for a large decrease in seawater strontium/calcium ratios and strontium concentrations during the Cenozoic: *Earth and Planetary Science Letters*, v. 282, p. 122–130, doi:[10.1016/j.epsl.2009.03.020](https://doi.org/10.1016/j.epsl.2009.03.020).
- Woodruff, F., Savin, S.M., and Douglas, R.G., 1981, Miocene Stable Isotope Record: A Detailed Deep Pacific Ocean Study and Its Paleoclimatic Implications: *Science*, v. 212, p. 665.
- Zachos, J.C., Dickens, G.R., and Zeebe, R.E., 2008, An early Cenozoic perspective on greenhouse warming and carbon-cycle dynamics: *Nature*, v. 451, p. 279–283, doi:[10.1038/nature06588](https://doi.org/10.1038/nature06588).

## Supplemental Data Repository

Isotope sclerochronology indicates enhanced seasonal precipitation in northern South America (Colombia) during the Mid Miocene Climatic Optimum

*Scholz et al. 2020*

---

### **This Data Repository Contains:**

- Supplementary Discussion/Text
  - Locality information – Guajira Peninsula
  - Locality information – Other modern sites
  - Instrumental data – Global gridded datasets
  - Methods – Shell sampling
  - Methods – Isotopic sampling
- Supplementary Figures
  - Figure DR1 – Maps of locations used for gridded dataset analysis
  - Figure DR2 – Geologic map of Guajira Peninsula
  - Figure DR3 – Composite stratigraphic column
  - Figure DR4 – Shell sampling schematic
  - Figure DR5 – Correlation between  $\delta^{18}\text{O}$  and  $\delta^{13}\text{C}$  in all shells
  - Figure DR6 –  $\delta^{18}\text{O}$  and  $\delta^{13}\text{C}$  profiles of all shells
  - Figure DR7 – Comparison between  $\delta^{18}\text{O}$  range and environmental parameters
  - Figure DR8 – Comparison between  $\delta^{18}\text{O}$  range, shell size and lifespan
  - Figure DR9 – Seasonal variation in sea surface temperatures, ERSST v. 5
  - Figure DR10 –  $\delta^{13}\text{C}$  profiles of all shells
  - Figure DR11 - Correlation between range in  $\delta^{13}\text{C}$  and range in  $\delta^{18}\text{O}$
  - Figure DR12 – Correlation between  $\Delta\delta^{18}\text{O}_{\text{sw}}$  and precipitation
  - Figure DR13 – Raman spectroscopy spectra
- Supplementary Tables
  - Table DR1 – Sample IDs, STRI locality numbers, stratigraphic heights and calibrated ages for all measured specimens.
  - Table DR2 – Raw  $\delta^{18}\text{O}$  and  $\delta^{13}\text{C}$  data for all shells [Separate Excel File]
  - Table DR3 – Shell lifespan, size, and  $\delta^{18}\text{O}$  and  $\delta^{13}\text{C}$  range for all shells
  - Table DR4 – Modern climate data for all sites
  - Table DR5 – SEM imagery
- Additional References not cited in the main text

## **Supplementary Discussion – Sample Locality Information**

### **GUAJIRA PENINSULA:**

Fossil samples were collected from various locations on the Guajira Peninsula from the Castilletes and Jimol Formations. These locations and sections are well described in other publications (Hendy et al., 2015; Moreno et al., 2015). Figures DR1 and DR2 in this supplement show a composite stratigraphic column displaying horizons from which fossil shells were collected, and a geologic map of the Peninsula with spatial distribution of sampling locations marked. Two modern samples were collected from coastal site 290628 (Figure DR2). The modern isotopic difference between continental precipitation and seawater in this region is 4-6‰ (IAEA/WMO 2018).

### **OTHER MODERN LOCATIONS:**

Modern turrillids collected at other tropical sites nearby the fossil collection site on the Guajira Peninsula were chosen from the dry collections of the Museum of Zoology Research Museum Collections at University of Michigan. These shells were collected by varying donors over many years, and were often part of personal collections before being donated to the museum. Therefore, specific location data (e.g. a specific beach or town) was often not available. However, all shells had a country of origin at a minimum, and in some cases more information such as a nearby city. The representations on the map in Figure 1 represent our best guess as to the location of sample collection based on the limited data available, but some of these locations have significant uncertainties. This uncertainty in location is mitigated by comparing isotope profiles to satellite-derived sea surface and precipitation data, which average over a larger area and reflect regional conditions.

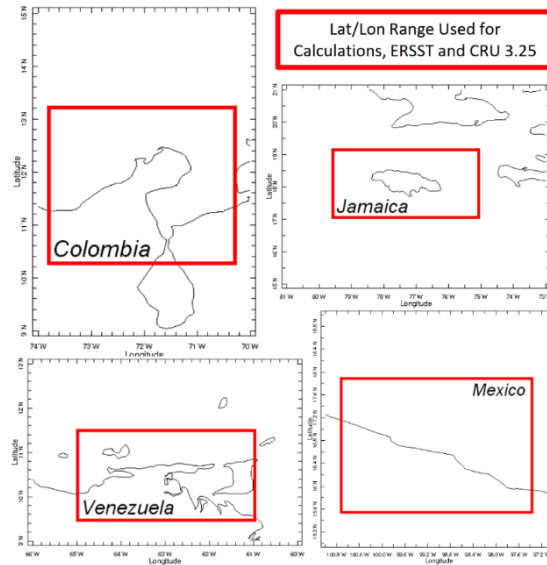
## **Supplementary Discussion – Instrumental Data**

### **GRIDDED DATASET SEA SURFACE TEMPERATURE (SST) AND PRECIPITATION DATA:**

Annual change and mean SST were calculated from NOAA ERSST v.5 dataset (Huang et al., 2017), over the regions shown in the maps to the right and below, highlighted by the red boxes. The same regions were used in calculation of precipitation data from the CRU 3.25 Global Precipitation dataset (Harris et al., 2014). In both cases, the region was averaged over using a latitude-weighted X-Y average, and the average monthly value was calculated for the period 1930-2012. Ranges in SST and precipitation were determined as the minimum to maximum monthly mean value. MAP was calculated by summing these means; seasonal variance was calculated by taking the difference of the highest and lowest (rainiest and driest, or warmest and coldest) months.

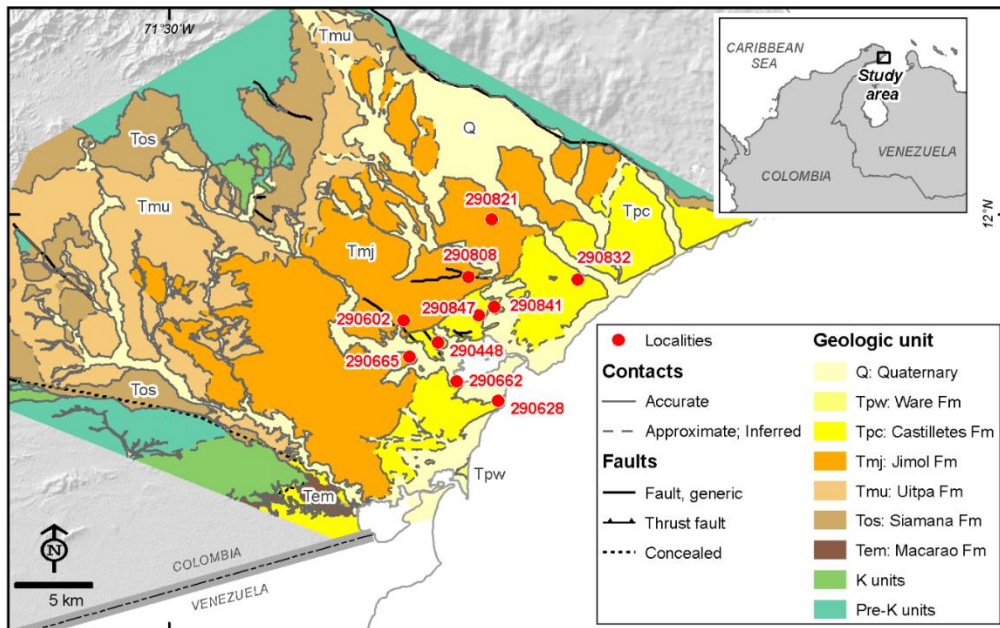
**Data Repository Figure 1 (DR1) –  
Locations Used for Calculations with Gridded Datasets (right)**

Red boxes show the latitude/longitude range defined for each modern site and carried forward into calculations of monthly average SSTs (NOAA ERSST v.5) and precipitation (CRU 3.25). The CRU 3.25 Global Precipitation dataset resolution is  $0.5^\circ \times 0.5^\circ$ , and the ERSST v.5 resolution is  $2^\circ \times 2^\circ$ .



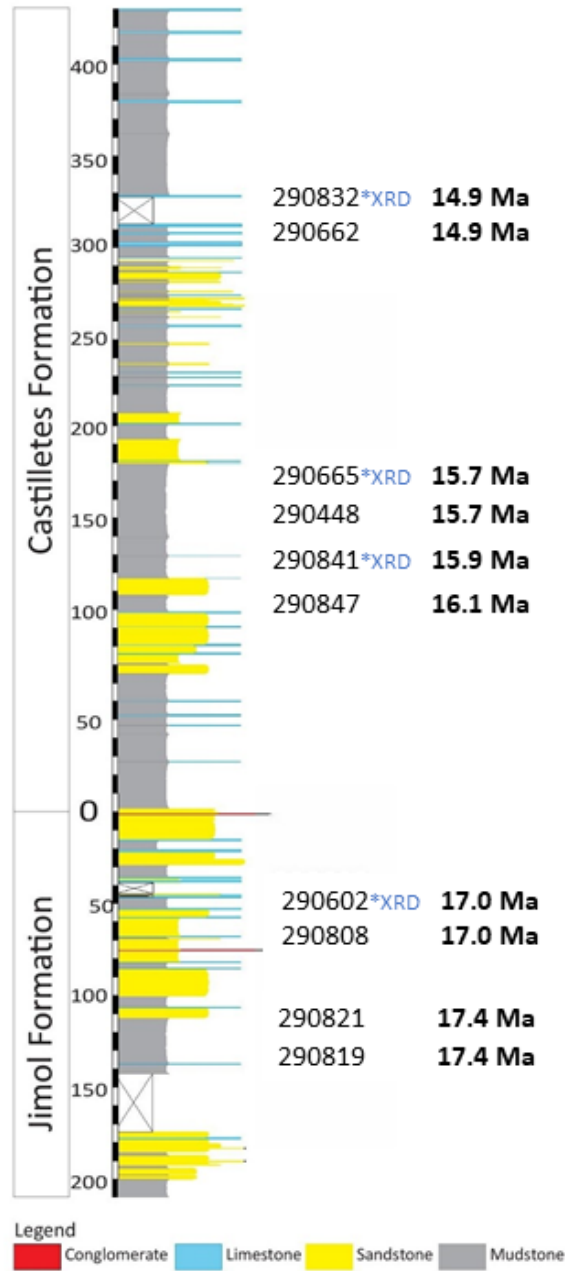
**Data Repository Figure 2 (DR2) – Geologic map of Guajira Peninsula with sampling locations**

Geologic map of the sampling locations on the Guajira Peninsula, Colombia. Numbers are the STRI locality IDs, which correspond to the names of samples collected at that location. The modern samples were collected at coastal site 290628. Modified from Moreno et al., 2015.



**Data Repository Figure 3 (DR3) – Composite stratigraphic column with sample horizons**

Composite stratigraphic column of the Jimol and Castilletes formation on the Guajira Peninsula, with labeled horizons showing the positions within the stratigraphy from which the 25 fossil *Turitella* samples were collected. Samples marked with \*XRD are levels in the stratigraphy where samples underwent X-ray diffraction to assess preservation (not on the same samples as were analyzed for stable isotopes).





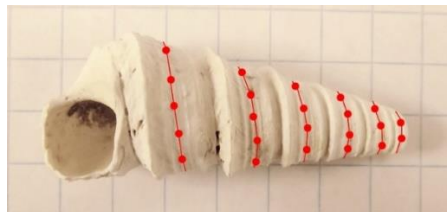
## Supplementary Discussion - Methods

### SHELL SAMPLING:

Shells were sampled along the spiral growth direction, while recording cumulative distance from the apex for each sampling location. Each sample was taken from the middle of the whorl, equidistant to each side. The high-resolution sampling scheme is illustrated in the photo below (Figure DR1). When the apex tip was broken, missing shell length was estimated using the Theoretical Apex System (TAS) method (Johnson et al., 2017), as employed by Anderson et al., (2017). 28 specimens underwent high-resolution drilling (3-12 samples/whorl, 40-50 $\mu$ g/sample), and 6 were sampled at coarser resolution (1 sample/whorl, ~10-40  $\mu$ g/sample) using a handheld drill at low speed. All sampled carbonate powders were analyzed for their stable isotopic composition ( $\delta^{18}\text{O}$  and  $\delta^{13}\text{C}$ ). Based on resulting  $\delta^{18}\text{O}$  cyclicity, shell lifespans were estimated to vary between <1 to 2 years as a minimum estimate (Table DR2), in agreement with previous studies of *Turritella* (Allmon, 2011; Anderson et al., 2017).

### Data Repository Figure 4 (DR4) – Shell sampling schematic

Sampling method along the center of each whorl, as demonstrated with sample 290602-A. Sample is on 1cm graph paper for scale.



### PRESERVATION ASSESSMENT:

Raman spectroscopy was used on all fossil shells and one modern shell, and showed spectral peaks corresponding to pure aragonite (see figure DR13). SEM imagery was taken of 13 fossil shells, spanning all ages and horizons, and showed the original aragonite shell fabric was intact, and similar in structure to modern samples (see Table DR5). Shells from four horizons were analyzed for XRD and were found to contain 100% aragonite.

Shells also preserve sinusoidal seasonal patterns in  $\delta^{18}\text{O}$  that are unlikely to survive significant alteration. Partial recrystallization or contamination with secondary material would, if anything, mute the seasonal magnitude seen in  $\delta^{18}\text{O}$  through regression to the mean: so, our conclusions about the increased magnitude in  $\delta^{18}\text{O}$  seen in fossil shells compared to modern should be robust to minor alteration.

### ISOTOPIC MEASUREMENTS:

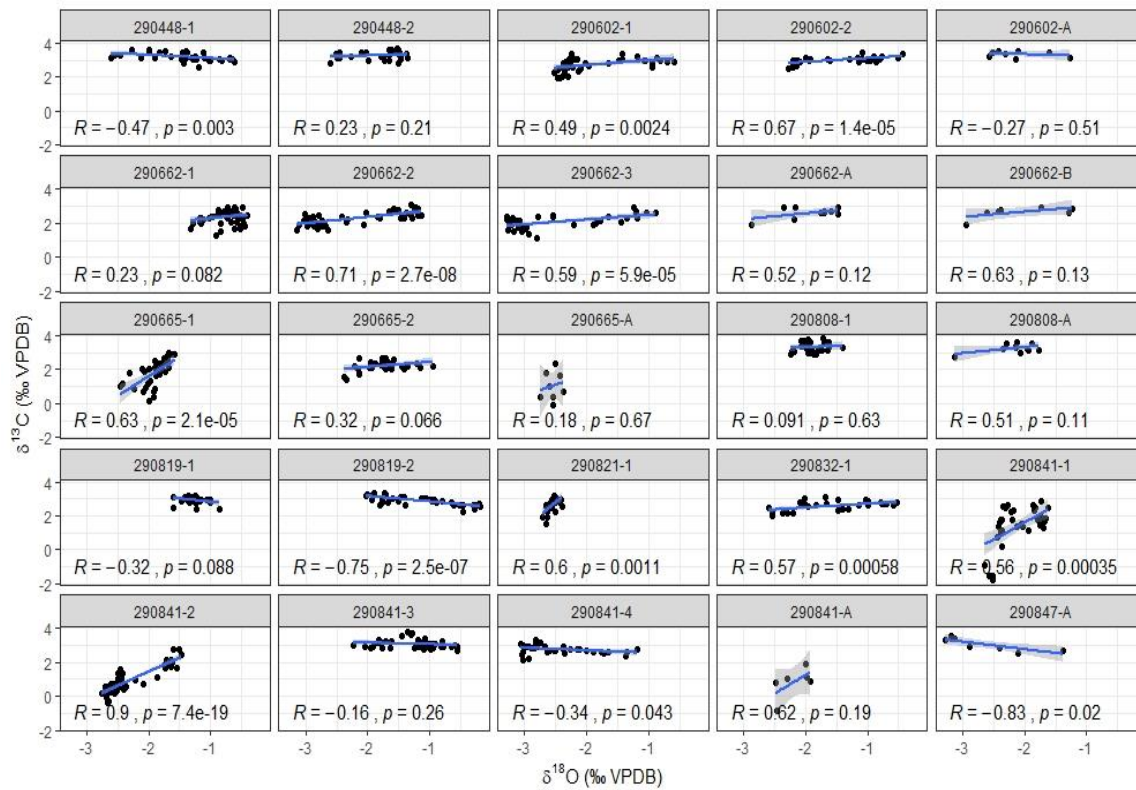
Stable isotopic analysis was conducted at both the University of Michigan and University of Florida. At University of Florida, samples were analyzed using a Kiel III carbonate preparation device attached to a Finnigan-MAT 252 mass spectrometer, with analytical error estimated to be  $\pm 0.03\text{‰}$  for  $\delta^{13}\text{C}$  and  $\pm 0.05\text{‰}$  for  $\delta^{18}\text{O}$  ( $n = 175$ ) based on calibration to daily analysis of NBS-19. At University of Michigan, samples were analyzed using a Kiel IV device attached to a Thermo-MAT 253 mass spectrometer and were calibrated against NBS-19 and

NBS-18 run daily. Analytical error on these measurements was better than  $\pm 0.1\%$  for both  $\delta^{13}\text{C}$  and  $\delta^{18}\text{O}$ . All  $\delta^{13}\text{C}$  and  $\delta^{18}\text{O}$  data are presented relative to Vienna Pee Dee Belemnite (VPDB).

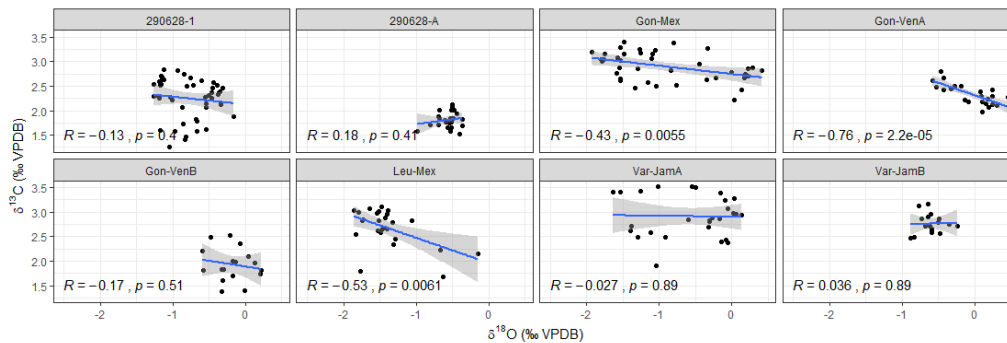
### Data Repository Figure 5 (DR5) – Correlation between $\delta^{18}\text{O}$ and $\delta^{13}\text{C}$ for all shells

Correlation of  $\delta^{18}\text{O}$  and  $\delta^{13}\text{C}$  values for all (A) fossil and (B) modern samples. Gray shaded area around each regression line represents the standard error of the fit. Out of 25 fossil shells analyzed, 9 showed significant positive correlation between  $\delta^{18}\text{O}$  and  $\delta^{13}\text{C}$ , 4 showed significant negative correlation, and 12 had correlations that were not significant at the 0.05  $p$ -value level. 18 out of the 25 shells (72%) show positive R values, which may indicate that they are influenced by freshening (Tao et al., 2013).

#### 5A) Fossil shells



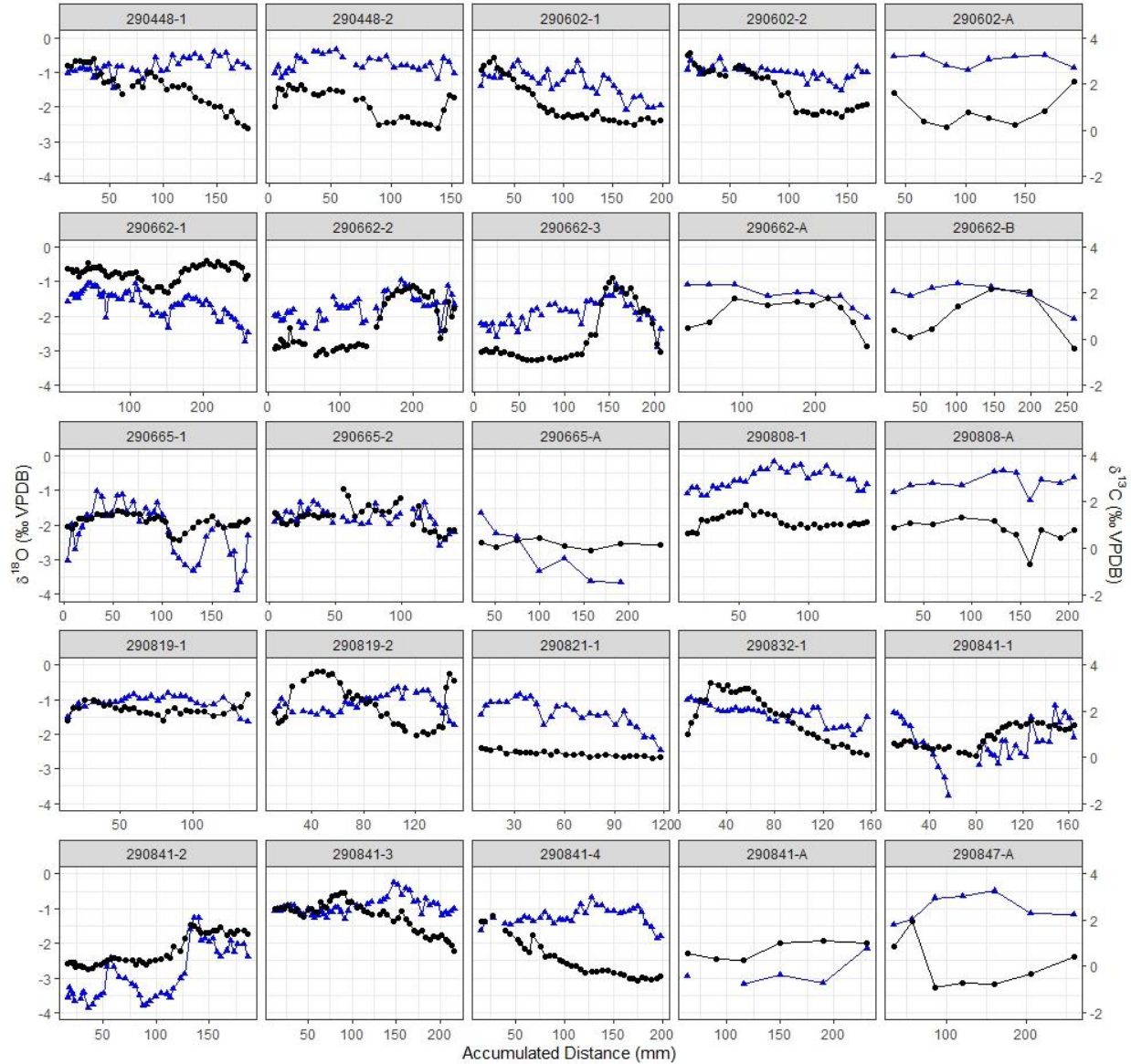
#### 5B) Modern shells



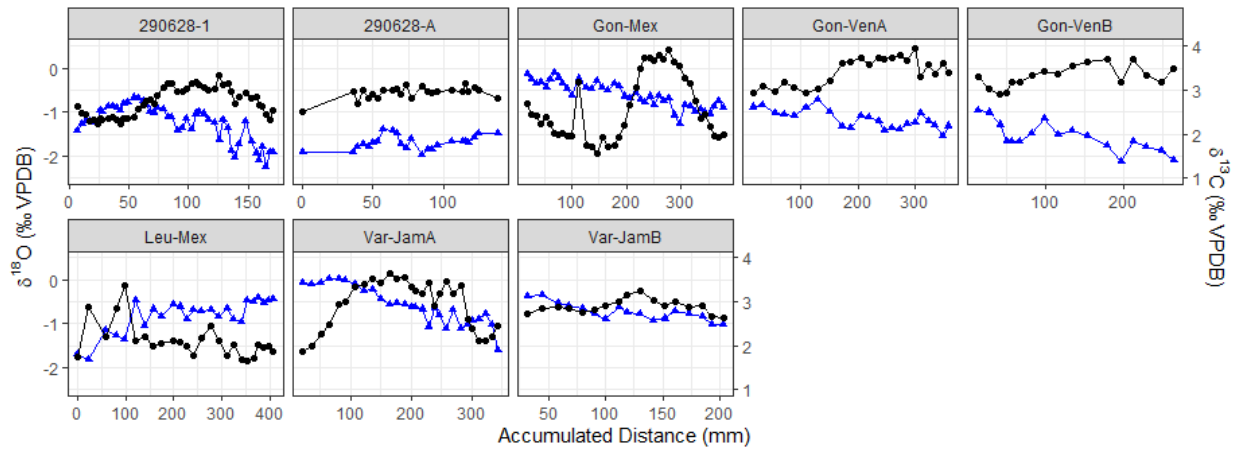
### Data Repository Figure 6 (DR6) – $\delta^{18}\text{O}$ and $\delta^{13}\text{C}$ profiles for all shells

Individual  $\delta^{18}\text{O}$  and  $\delta^{13}\text{C}$  profiles for all (A) fossil and (B) modern samples, showing subannual variations.  $\delta^{18}\text{O}$  data (black circles) plotted on the left y-axis, with values inverted.  $\delta^{13}\text{C}$  data (blue line, triangles) plotted on the right y-axis (not inverted). X-axis shows the accumulated distance from the apex of the shell (0mm) to the aperture, along the spiral growth direction.

#### 6A) Fossil specimens



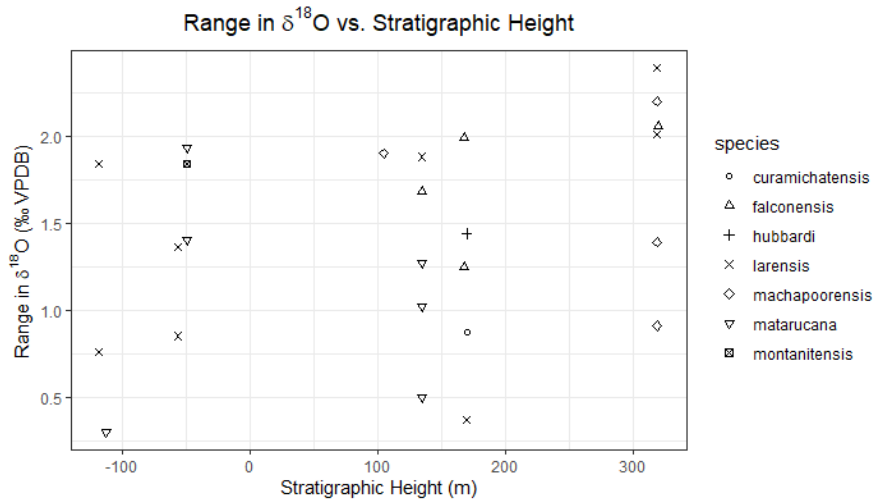
6B) Modern specimens



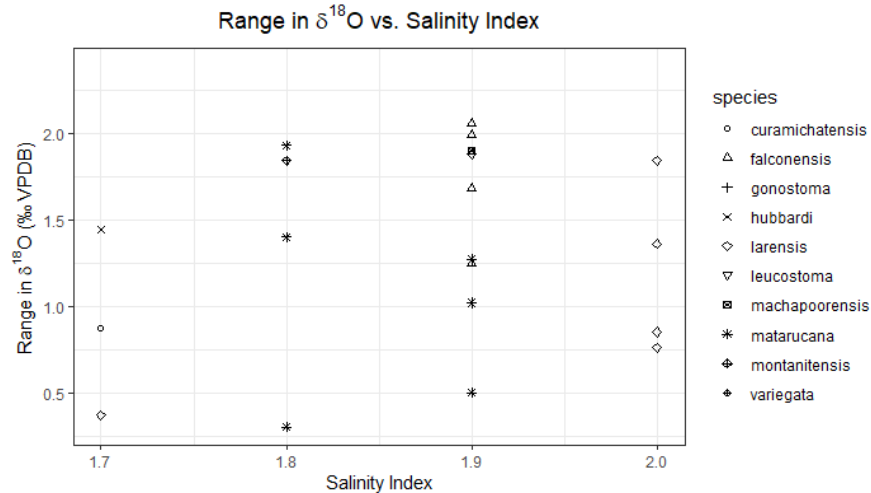
**Data Repository Figure 7 (DR7) – Comparison between  $\delta^{18}\text{O}$  range and environmental parameters**

Correlation between the range in  $\delta^{18}\text{O}$  in each specimen and (A) the shell's stratigraphic height, (B) the interpreted paleosalinity, or (C) the inferred paleodepth. Paleosalinity and paleodepth taken from Hendy et al., 2015.

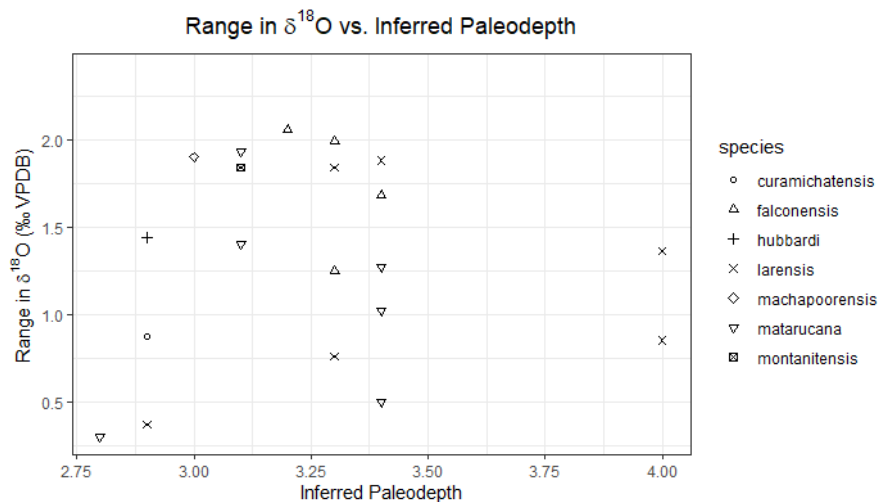
7A) Stratigraphic height vs. range in  $\delta^{18}\text{O}$  in each shell, showing no correlation. Shells showing high (>1.5‰) ranges in  $\delta^{18}\text{O}$  occur at all sampled horizons. Symbols represent the specific species of *Turritella*.



7B) Paleosalinity index vs.  $\delta^{18}\text{O}$  range, showing no correlation. Salinity is in arbitrary units where 1=estuarine and 2=fully marine, numbers between 1 and 2 are the result of averaging all species in a given horizon for a determination of ‘mostly marine’ or ‘mostly estuarine’. Paleosalinity values are taken from Hendy et al. 2015, and include more specimens than were analyzed here. Paleosalinity does not vary much below fully marine in the sampled horizons, and shells showing high ( $>1.5\%$ ) ranges in  $\delta^{18}\text{O}$  occur at 3 of 4 paleosalinity levels. Symbols represent the specific species of *Turritella*.

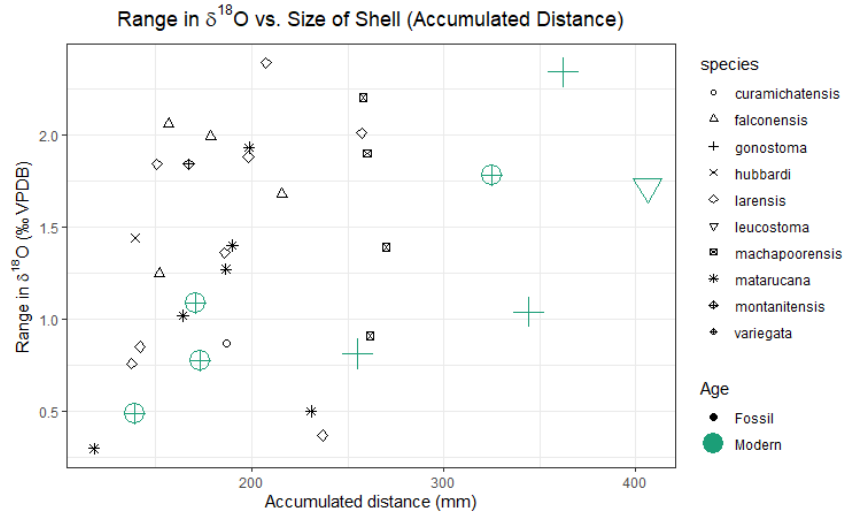


7C) Paleodepth index vs.  $\delta^{18}\text{O}$  range, showing no correlation. Depth index is in arbitrary units where 1=intratidal, 2=shoreface (0-5m), 3=nearshore (5-15m), 4=inner shelf (15-50m), 5=mid shelf (5-100m), and 6=outer shelf (100-200m). Our samples range from (far) shoreface to the inner shelf, with most between 3-3.5 (nearshore). Shells showing high ( $>1.5\%$ ) ranges in  $\delta^{18}\text{O}$  occur at most paleodepth levels (3-3.5), with potentially reduced ranges at deeper depths (paleodepth = 4), however there are only a small number of samples at this depth. Symbols represent the specific species of *Turritella*.

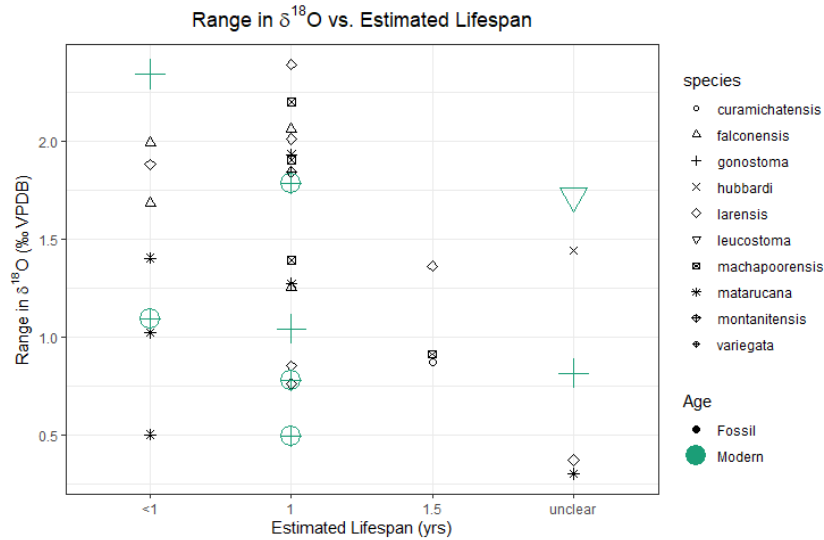


## Data Repository Figure 8 (DR8) – Comparison between $\delta^{18}\text{O}$ range, shell size and lifespan

8A) Shell size. Range in  $\delta^{18}\text{O}$  of each shell plotted against the total accumulated distance along the growth direction of each shell, a measurement of shell size, showing no correlation. Shells showing high ( $>1.5\%$ ) ranges in  $\delta^{18}\text{O}$  occur at all shell sizes between 150 and 375mm accumulated distance. Shells with accumulated distance less than 150mm show somewhat reduced range, although there are not many shells at this small size. Symbols represent the specific species of *Turritella*. There is not known to be any relationship between shell size and lifespan in turritellids (Allmon and Jones, 1992).



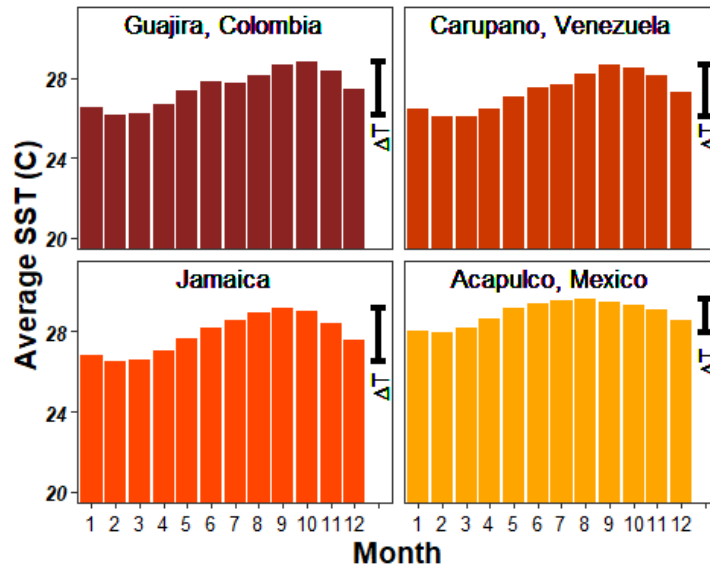
8B) Estimated lifespan. Range in  $\delta^{18}\text{O}$  of each shell plotted against the estimated lifespan, showing no correlation. Shell lifespans were estimated based on  $\delta^{18}\text{O}$  cyclicity, with the presence of a full sinusoid indicating a full year of life. Shell lifespans varied between  $<1$  to 1.5 years as a minimum estimate (Table DR2), in agreement with previous studies of *Turritella* (Allmon, 2011; Anderson et al., 2017). There is not known to be any relationship between shell size and lifespan in turritellids (Allmon and Jones, 1992). Symbols represent the specific species of *Turritella*.





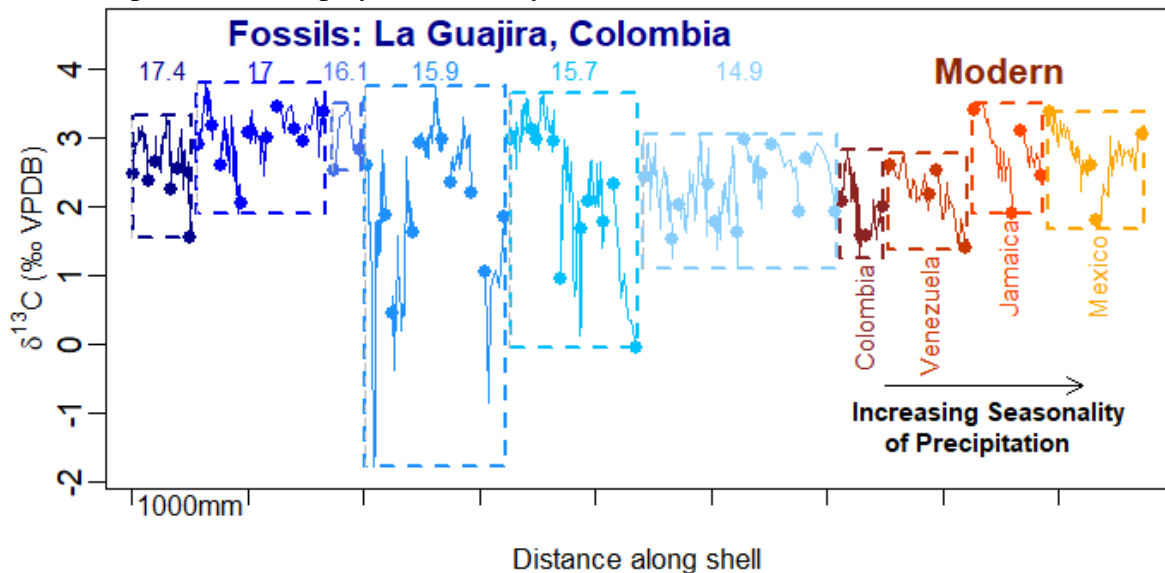
**Data Repository Figure 9 (DR9) – Seasonal variation in sea surface temperature at 4 modern sites**

Seasonal variation in sea surface temperature (SST, °C) by month at each of the four modern sites. Data calculated from the NOAA ERSST v.5 gridded dataset. SST was averaged across the region (latitude-weighted), and then averaged in each month from 1930-2012.



**Data Repository Figure 10 (DR10) –  $\delta^{13}\text{C}$  profiles of all shells**

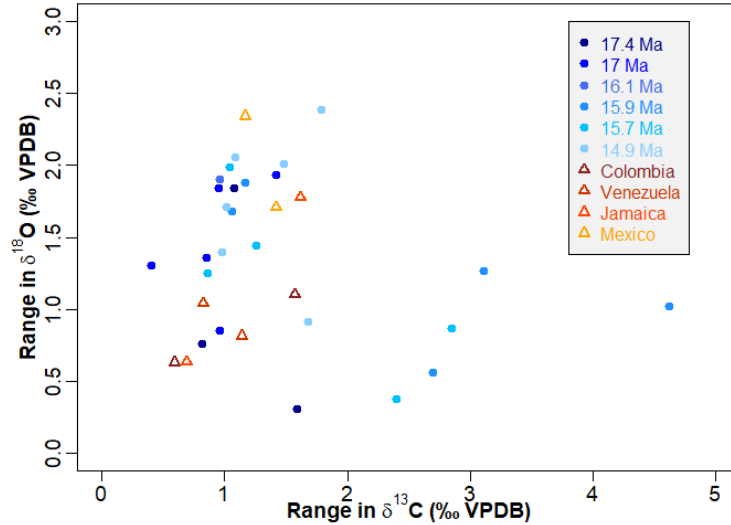
$\delta^{13}\text{C}$  sclerochronologies of all shells, plotted similar to Figure 2, which shows  $\delta^{18}\text{O}$ . Fossil shells are arranged based on age of horizon. Modern shells are arranged by location, first showing Guajira Peninsula, and then in order of increasing precipitation seasonality. Boxes show range of maximum to minimum  $\delta^{13}\text{C}$  for each modern location, or all fossil shells. X-axis represents the accumulated distance in the spiral direction around each shell: each shell's distance values were added to the previous to display them side by side. All values are in reference to VPDB.





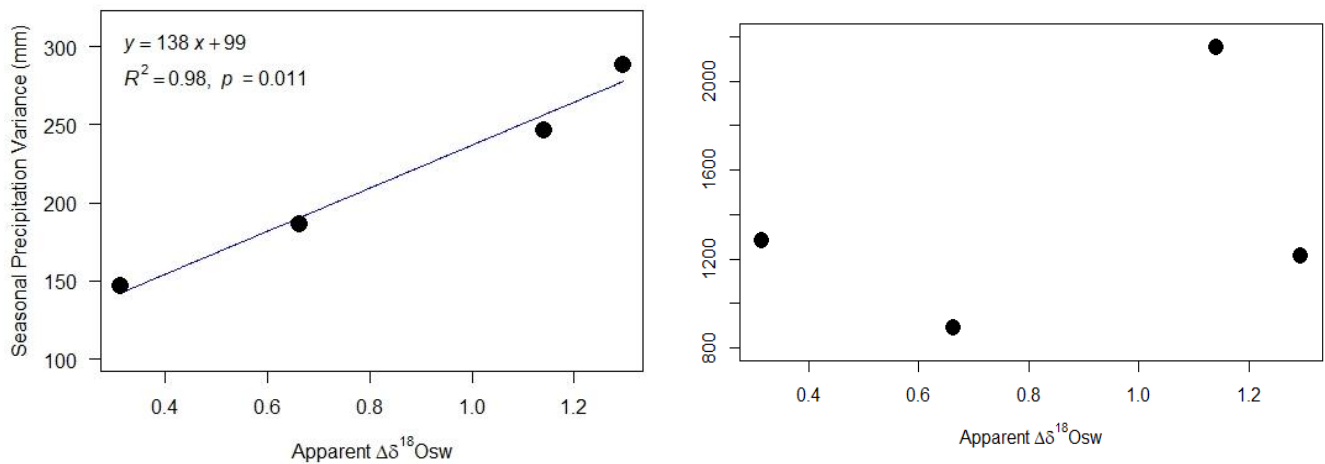
### Data Repository Figure 11 (DR11) – Correlation between range in $\delta^{13}\text{C}$ and range in $\delta^{18}\text{O}$

Correlation is shown between range in  $\delta^{13}\text{C}$  and range in  $\delta^{18}\text{O}$  for all fossil and modern shells. No statistically significant correlation present ( $R^2$  value of 0.01,  $p$ -value 0.24).



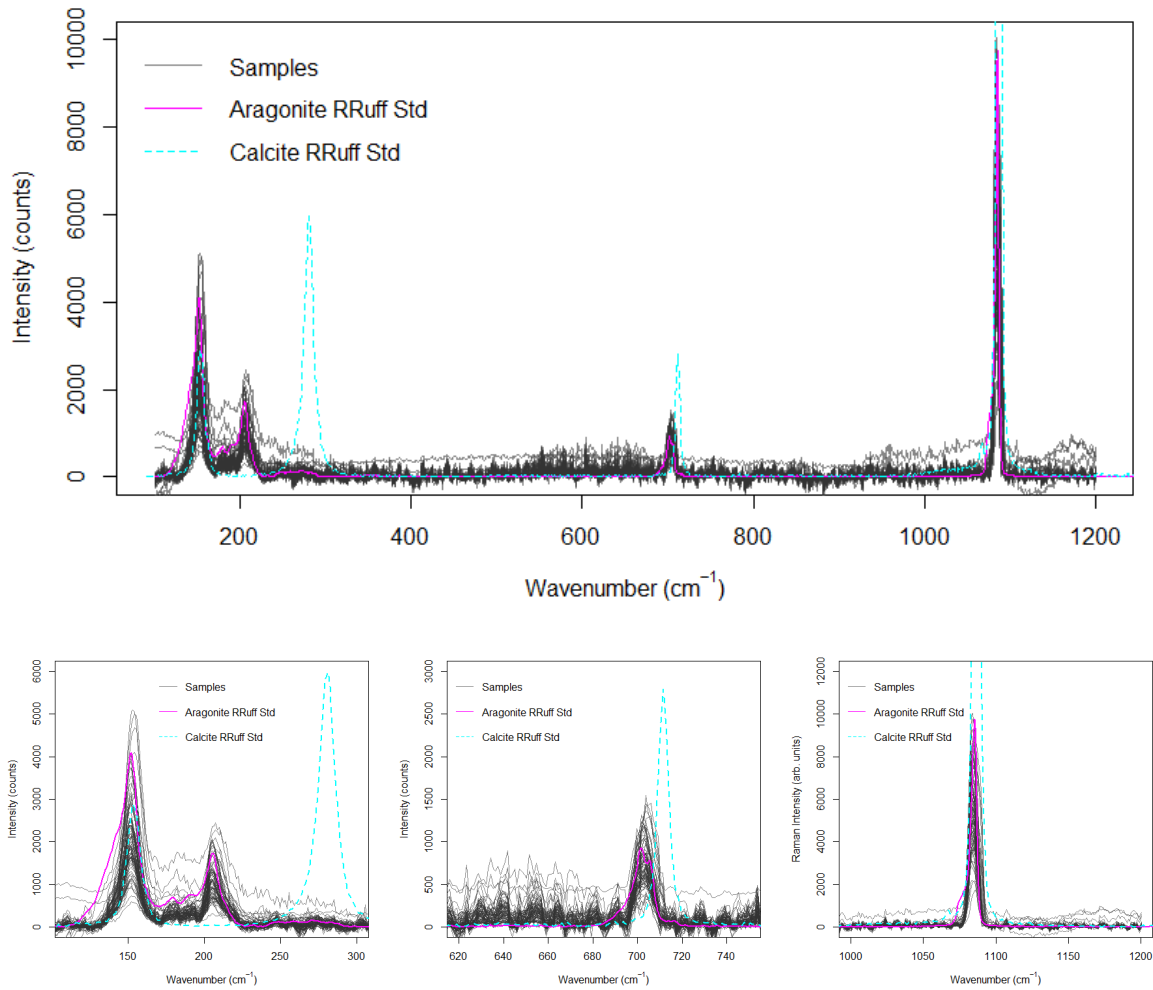
### Data Repository Figure 12 (DR12) – Correlation between apparent $\Delta\delta^{18}\text{O}_{\text{sw}}$ and Precipitation

Correlation is shown between apparent  $\Delta\delta^{18}\text{O}_{\text{sw}}$  and seasonal precipitation variance (left), and mean annual precipitation (MAP, right), at each of the four modern sites. There is no correlation between apparent  $\Delta\delta^{18}\text{O}_{\text{sw}}$  and MAP (right), but there is a strong correlation with seasonal precipitation variance (left). While four points is insufficient to be considered an empirically robust relationship, further research into this trend is warranted, as the strong correlation shows promise.



## Data Repository Figure 13 (DR13) – Raman spectroscopy of all samples

All fossil shells and 1 modern shell were scanned using Raman spectroscopy. We took point measurements using a Horiba XploRA PLUS Raman spectrometer paired with an Olympus BX41 microscope. The XploRA system is equipped with a 532 nm diode laser. We collected the spectra using a groove density of 1800 g/mm over a range of 100 to 1600  $\text{cm}^{-1}$  at a laser power output of  $\sim 10$  mW. We collected three scans per sample with a 3 second exposure time and 15 accumulations using a 50x long working distance objective. We used a polynomial baseline correction to remove background fluorescence in the LabSpec6 platform. The standards are sourced from the RRUFF database. Samples were mounted on microscope slides and stabilized in putty. Sample scans are included in the below figures as transparent gray lines. The RRuff standards for aragonite and calcite are plotted in pink and blue, respectively. All samples scanned had spectra clearly corresponding to aragonite, given the position and intensity of the peaks. The modern shell scans were not significantly different from fossil scans.



**Data Repository Table DR1 - Sample IDs, STRI locality numbers, stratigraphic heights and calibrated ages for all measured specimens.**

For samples collected on the Guajira peninsula (all fossil specimens and two modern), the sample name is structured as the STRI locality ID, followed by the specimen identifier, which is either a number if named by Universidad del Norte (UdN), or a letter if named by University of Michigan (UofM). Modern samples are in shaded gray cells. Sample not analyzed for stable isotopes and only used for XRD have a locality number followed by an X, and XRD is specified in the Resolution column. For modern *Turritella* specimen not collected on the Guajira peninsula, the sample name is a shorted form of the species and location (country) collected from.

Sample Name	Resolution	Locality STRI ID	Age	Calibrated Age	Unit	Strat. Height	Species	Location
290819-1	High	290819	Burdigalian	17.4	Jimol	-118	<i>T. larensis</i>	Guajira
290819-2	High	290819	Burdigalian	17.4	Jimol	-118	<i>T. larensis</i>	Guajira
290821-1	High	290821	Burdigalian	17.4	Jimol	-112	<i>T. matarucana</i>	Guajira
290808-1	High	290808	Burdigalian	17.0	Jimol	-56	<i>T. larensis</i>	Guajira
290602-1	High	290602	Burdigalian	17.0	Jimol	-49	<i>T. matarucana</i>	Guajira
290602-2	High	290602	Burdigalian	17.0	Jimol	-49	<i>T. montanitensis</i>	Guajira
290841-1	High	290841	Langhian	15.9	Castilletes	135	<i>T. matarucana</i>	Guajira
290841-2	High	290841	Langhian	15.9	Castilletes	135	<i>T. matarucana</i>	Guajira
290841-3	High	290841	Langhian	15.9	Castilletes	135	<i>T. falconensis</i>	Guajira
290841-4	High	290841	Langhian	15.9	Castilletes	135	<i>T. larensis</i>	Guajira
290448-1	High	290448	Langhian	15.7	Castilletes	168	<i>T. falconensis</i>	Guajira
290448-2	High	290448	Langhian	15.7	Castilletes	168	<i>T. falconensis</i>	Guajira
290665-1	High	290665	Langhian	15.7	Castilletes	170	<i>T. curamichatensis</i>	Guajira
290665-2	High	290665	Langhian	15.7	Castilletes	170	<i>T. hubbardi</i>	Guajira
290662-1	High	290662	Langhian	14.9	Castilletes	319	<i>T. machapoorensis</i>	Guajira
290662-2	High	290662	Langhian	14.9	Castilletes	319	<i>T. larensis</i>	Guajira
290662-3	High	290662	Langhian	14.9	Castilletes	319	<i>T. larensis</i>	Guajira
290832-1	High	290832	Langhian	14.9	Castilletes	320	<i>T. falconensis</i>	Guajira
290602-A	Coarse	290602	Burdigalian	17.0	Jimol	-49	<i>T. matarucana</i>	Guajira
290662-A	Coarse	290662	Langhian	14.9	Castilletes	319	<i>T. machapoorensis</i>	Guajira
290662-B	Coarse	290662	Langhian	14.9	Castilletes	319	<i>T. machapoorensis</i>	Guajira
290665-A	Coarse	290665	Langhian	15.7	Castilletes	170	<i>T. larensis</i>	Guajira
290808-A	Coarse	290808	Burdigalian	17.0	Jimol	-56	<i>T. larensis</i>	Guajira
290841-A	Coarse	290841	Langhian	15.9	Castilletes	135	<i>T. matarucana</i>	Guajira
290847-A	Coarse	290847	Burdigalian	16.1	Castilletes	105	<i>T. machapoorensis</i>	Guajira
290628-1	High	290628	Modern	Modern	Modern	Modern	<i>T. variegata</i>	Guajira
290628-A	High	290628	Modern	Modern	Modern	Modern	<i>T. variegata</i>	Guajira
Gon-Mex	High	N/A	Modern	Modern	Modern	Modern	<i>T. gonostoma</i>	Mexico
Leu-Mex	High	N/A	Modern	Modern	Modern	Modern	<i>T. leucostoma</i>	Mexico
Gon-VenA	High	N/A	Modern	Modern	Modern	Modern	<i>T. gonostoma</i>	Venezuela
Gon-VenB	High	N/A	Modern	Modern	Modern	Modern	<i>T. gonostoma</i>	Venezuela
Var-JamA	High	N/A	Modern	Modern	Modern	Modern	<i>T. variegata</i>	Jamaica
Var-JamB	High	N/A	Modern	Modern	Modern	Modern	<i>T. variegata</i>	Jamaica
290602-X	XRD	290602	Burdigalian	17.0	Jimol	-49	<i>T. matarucana</i>	Guajira
290841-X	XRD	290841	Langhian	15.9	Castilletes	135	<i>T. matarucana</i>	Guajira
290665-X	XRD	290665	Langhian	15.7	Castilletes	170	<i>T. curamichatensis</i>	Guajira
290832-X	XRD	290832	Langhian	14.9	Castilletes	320	<i>T. machapoorensis</i>	Guajira

## Data Repository Table DR2 – Raw $\delta^{18}\text{O}$ and $\delta^{13}\text{C}$ data for all shells

All individual  $\delta^{18}\text{O}$  and  $\delta^{13}\text{C}$  values are included in a supplementary Excel table.

## Data Repository Table DR3 – Shell lifespan, size, and $\delta^{18}\text{O}$ and $\delta^{13}\text{C}$ range for all shells

This table contains columns for sample number, *Turritella* species, estimated lifespan, size (represented by total spiral distance around the shell), and max-to-min range in  $\delta^{18}\text{O}$  and  $\delta^{13}\text{C}$ . Cells shaded gray are modern samples.

Sample Name	Species	Lifespan (yrs)	Total acc. distance (mm)	$\delta^{13}\text{C}$ range (‰ VPDB)	$\delta^{18}\text{O}$ range (‰ VPDB)
290819-1	<i>T. larensis</i>	1	137.4	0.80	0.76
290819-2	<i>T. larensis</i>	1	150.6	1.08	1.84
290821-1	<i>T. matarucana</i>	unclear	118.0	1.59	0.30
290808-1	<i>T. larensis</i>	1	141.9	0.96	0.85
290602-1	<i>T. matarucana</i>	1	198.6	1.42	1.93
290602-2	<i>T. montanitensis</i>	1	167.1	0.95	1.84
290841-1	<i>T. matarucana</i>	<1	164.1	4.62	1.02
290841-2	<i>T. matarucana</i>	1	186.5	3.11	1.27
290841-3	<i>T. falconensis</i>	<1	215.8	1.06	1.68
290841-4	<i>T. larensis</i>	<1	198.3	1.17	1.88
290448-1	<i>T. falconensis</i>	<1	178.7	1.04	1.99
290448-2	<i>T. falconensis</i>	1	152.0	0.86	1.25
290665-1	<i>T. curamichatensis</i>	1.5	186.7	2.85	0.87
290665-2	<i>T. hubbardi</i>	unclear	139.6	1.26	1.44
290662-1	<i>T. machapoorensis</i>	1.5	261.6	1.68	0.91
290662-2	<i>T. larensis</i>	1	257.2	1.50	2.01
290662-3	<i>T. larensis</i>	1	207.4	1.79	2.39
290832-1	<i>T. falconensis</i>	1	156.9	1.09	2.06
290602-A	<i>T. matarucana</i>	<1	190.0	0.60	1.40
290662-A	<i>T. machapoorensis</i>	<1	270.0	0.98	1.39
290662-B	<i>T. machapoorensis</i>	1	258.0	1.01	2.20
290665-A	<i>T. larensis</i>	unclear	237.0	2.35	0.37
290808-A	<i>T. larensis</i>	1.5	186.0	0.8	1.36
290841-A	<i>T. matarucana</i>	<1	231.0	2.70	0.50
290847-A	<i>T. machapoorensis</i>	1	260.0	0.96	1.90
290628-1	<i>T. variegata</i>	1	171.0	1.58	1.09
290628-A	<i>T. variegata</i>	<1	139.0	0.25	0.49
Gon-Mex	<i>T. gonostoma</i>	1	362.0	1.18	2.34
Leu-Mex	<i>T. leucostoma</i>	unclear	406.0	1.42	1.72
Gon-VenA	<i>T. gonostoma</i>	1	344.0	0.83	1.04
Gon-VenB	<i>T. gonostoma</i>	unclear	255.0	1.14	0.81
Var-JamA	<i>T. variegata</i>	1	325.0	1.66	1.78
Var-JamB	<i>T. variegata</i>	<1	173.0	0.76	0.78

### Data Repository Table DR4 – Modern climate data for all sites

Air temperature data was obtained for several nearby stations to the sampling site, and is based on NOAA Daily Summaries (Venezuela, Jamaica and Mexico) and IDEAM historical data (Colombia). Sea surface temperature data was obtained from instrumental records (see sources below table), was also calculated using the ERSST v. 5 global gridded model for comparison (Huang et al., 2017). Calculations were made by averaging by month over the period 1930-2012, and the resulting range is the average seasonal temperature range. The same time period was used to determine precipitation from the CRU 3.25 Global Precipitation dataset (Harris et al., 2014). Seasonal variance in air temperature ( $\Delta T$ ), SSTs ( $\Delta SST$ ) and precipitation (seasonal variance) was calculated by taking the difference of the highest and lowest average monthly values.

Location	Air Temperature Data: NOAA Daily Summaries, IDEAM Historical Data			SSTs: Local, Instrumental Data		SSTs: ERSST v.5 Gridded Dataset		Precipitation: CRU 3.25 Gridded Dataset	
	MAT (°C)	Seasonal T Range	$\Delta T$ Annual	Seasonal T Range	$\Delta SST$ Annual	Mean annual SST	$\Delta SST$ Annual	MAP (mm)	seasonal variance (mm)
<b>Castilletes, La Guajira, CO</b>	<b>28.2</b>	<b>26.8-29.1</b>	<b>2.3</b>	<b>24.9-27.9</b> (a)	<b>3.0</b>	<b>27.5</b>	<b>2.65</b>	<b>892</b>	<b>186</b>
Nazareth, CO	27.1	25.7-27.8	2.1						
Pto Bolivar, CO	28.4	27.0-29.3	2.3						
Rancho Grande, CO	29	27.8-29.9	2.1						
<b>Carupano, VE</b>	<b>27.5</b>	<b>26.3-28.3</b>	<b>2</b>	<b>23.4-26.8</b> (b)	<b>3.4</b>	<b>27.3</b>	<b>2.58</b>	<b>1282</b>	<b>147</b>
Antonio Jose de Sucre, VE	27.6	26.6-28.4	1.8						
Guiria, VE	27.7	26.6-28.5	1.9						
Piarco Intl Airport, TD	27.1	26.0-27.8	1.8						
Porlamar Intl Airport, VE	27.7	26.0-28.4	2.4						
<b>Jamaica</b>	<b>27.4</b>	<b>25.9-28.8</b>	<b>2.9</b>	<b>26.5-29.5</b> (c)	<b>3.0</b>	<b>27.9</b>	<b>2.65</b>	<b>2153</b>	<b>246</b>
Montego Bay, JM	27	25.4-28.3	2.9						
Norman Manley Intl, JM	27.8	26.3-29.3	2.9						
<b>Acapulco, MX</b>	<b>27.7</b>	<b>26.5-28.9</b>	<b>2.4</b>	<b>25.6-30.5</b> (d)	<b>4.9</b>	<b>28.9</b>	<b>2.1</b>	<b>1215</b>	<b>288</b>

(a) Montoya-Sánchez et al., 2018

(b) Jury, 2018

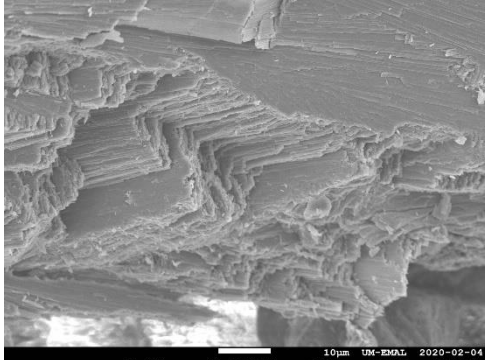
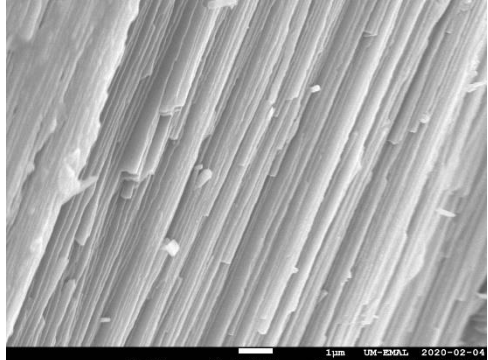
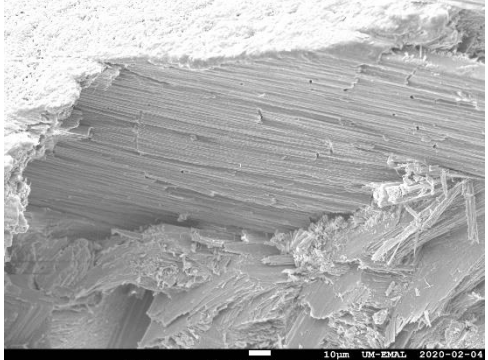
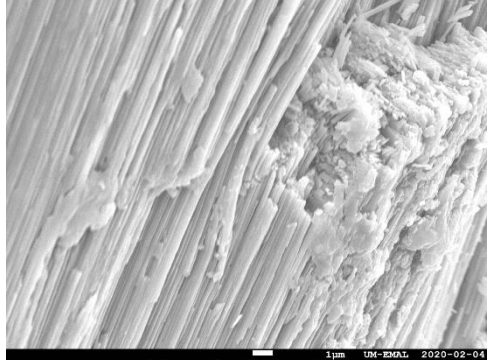

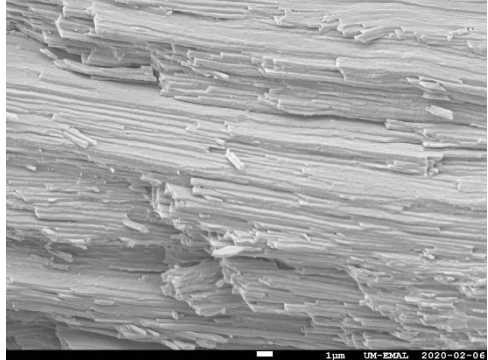
(c) Gates, 1990

(d) Rojas-Herrera et al., 2016; Moreno-Díaz et al., 2015

NOAA\_ERSST\_V5 data provided by the NOAA/OAR/ESRL PSD, Boulder, Colorado, USA, at their website <https://www.esrl.noaa.gov/psd/>

**Data Repository Table DR5 – SEM imagery**

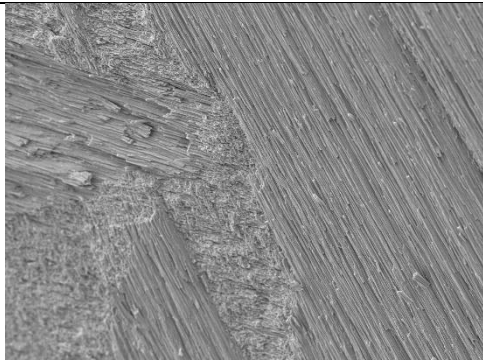
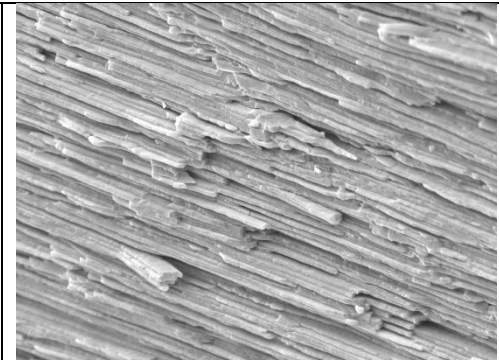
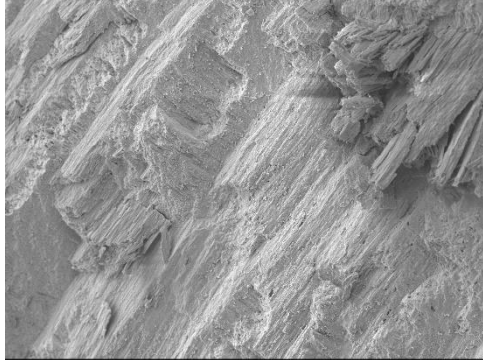
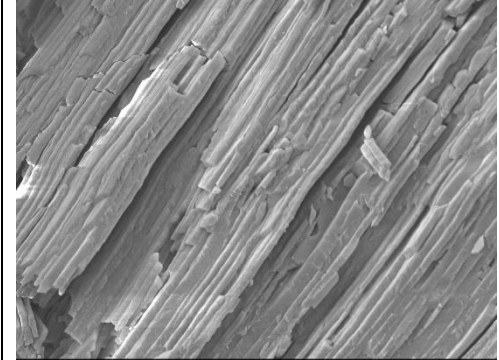
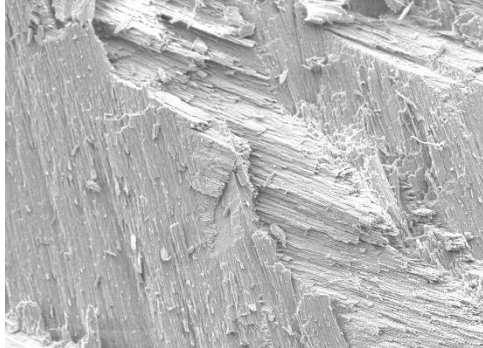
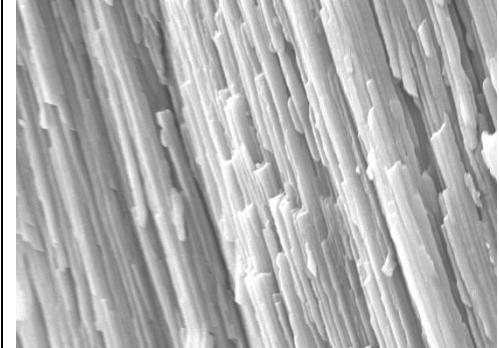
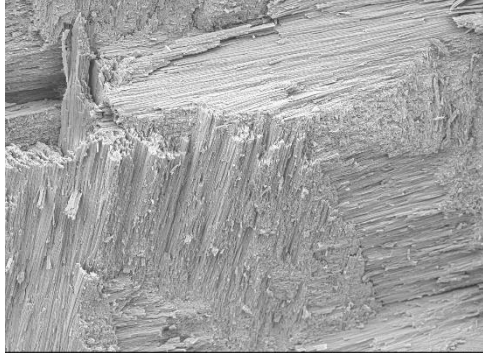
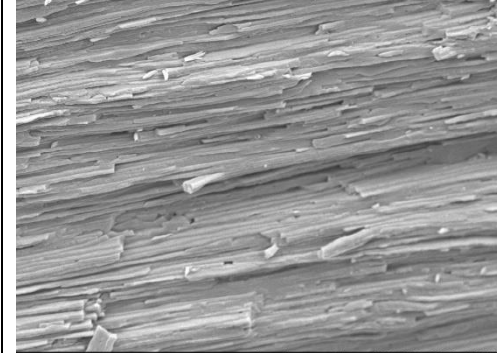
SEM imagery of fossil samples showed preservation of the original aragonitic shell fabric, which is visually very similar to the fabric observed in modern samples (top 3 rows). Fossil samples also preserve larger-scale cross-lamellar growth patterns, common in gastropods, and documented in the left column of images. Both of these structures are indicative of original, biogenic aragonite. Images were taken on a freshly broken face, broken off from near the shell aperture.

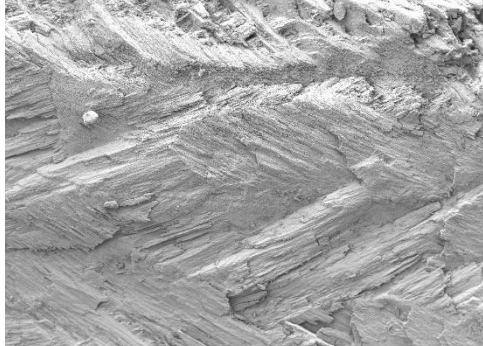
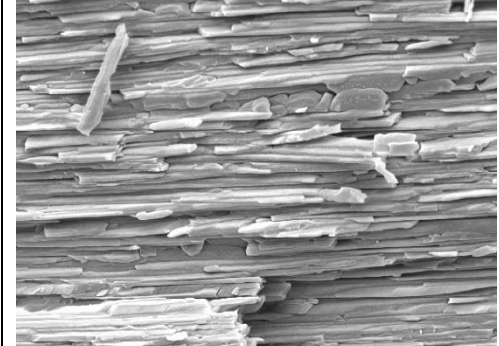
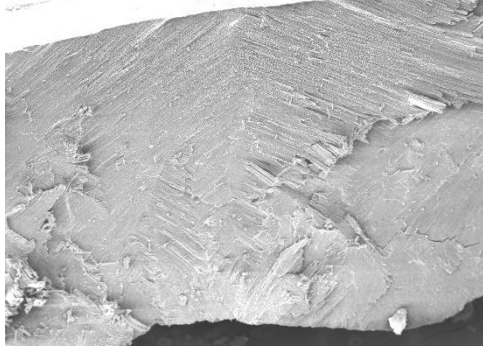
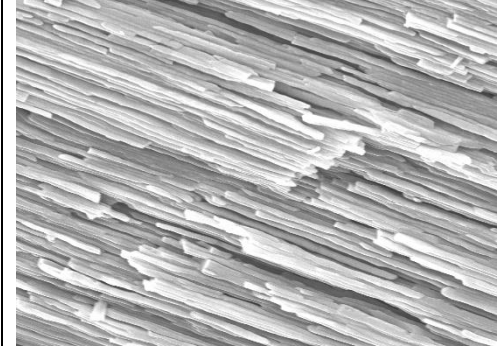
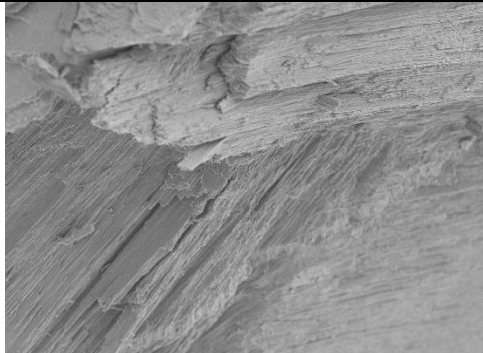
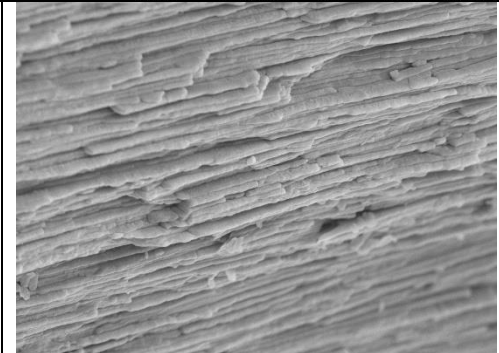
Sample name	Image 1 (cross-lamellar growth pattern)	Image 2 (detail of shell fabric)
290628-1 (modern)	 <p>SEM image showing cross-lamellar growth pattern. Magnification: x1,300. Scale bar: 10µm. Metadata: UM-EMAL, 2020-02-04, 10.0kV LED, SEM, WD 9mm, 11:41:37.</p>	 <p>SEM image showing detail of shell fabric. Magnification: x8,500. Scale bar: 1µm. Metadata: UM-EMAL, 2020-02-04, 10.0kV LED, SEM, WD 10mm, 12:08:29.</p>
290628-A (modern)	 <p>SEM image showing cross-lamellar growth pattern. Magnification: x550. Scale bar: 10µm. Metadata: UM-EMAL, 2020-02-04, 10.0kV LED, SEM, WD 10mm, 11:23:08.</p>	 <p>SEM image showing detail of shell fabric. Magnification: x5,000. Scale bar: 1µm. Metadata: UM-EMAL, 2020-02-04, 10.0kV LED, SEM, WD 10mm, 11:25:50.</p>
Var-JamB (modern)	 <p>SEM image showing cross-lamellar growth pattern. Magnification: x170. Scale bar: 100µm. Metadata: UM-EMAL, 2020-02-06, 5.0kV LED, SEM, WD 11mm, 11:14:41.</p>	 <p>SEM image showing detail of shell fabric. Magnification: x4,000. Scale bar: 1µm. Metadata: UM-EMAL, 2020-02-06, 5.0kV LED, SEM, WD 11mm, 11:10:06.</p>



<p>290448-1</p>		
<p>290602-1</p>		
<p>290662-3</p>		
<p>290662-A</p>		



<p>290665- A</p>	 <p>x1,900 5.0kV LED SEM 10µm UM-EMAL 2020-02-06 WD 10mm 11:49:02</p>	 <p>x11,000 5.0kV LED SEM 1µm UM-EMAL 2020-02-06 WD 10mm 11:52:03</p>
<p>290808- 1</p>	 <p>x950 5.0kV LED SEM 10µm UM-EMAL 2020-02-06 WD 10mm 11:32:30</p>	 <p>x7,000 5.0kV LED SEM 1µm UM-EMAL 2020-02-06 WD 10mm 11:34:05</p>
<p>290819- 1</p>	 <p>x300 10.0kV LED SEM 10µm UM-EMAL 2020-02-06 WD 10mm 11:47:14</p>	 <p>x11,000 10.0kV LED SEM 1µm UM-EMAL 2020-02-06 WD 10mm 11:51:53</p>
<p>290821- 1</p>	 <p>x1,500 5.0kV LED SEM 10µm UM-EMAL 2020-02-06 WD 10mm 11:23:02</p>	 <p>x6,500 5.0kV LED SEM 1µm UM-EMAL 2020-02-06 WD 10mm 11:20:55</p>

<p>290832-1</p>		
<p>290841-1</p>	 <p data-bbox="454 903 828 934"> <small>x130 10.0kV LED SEM WD 9mm 12:13:46 100µm UM-EMAL 2020-02-04</small> </p>	 <p data-bbox="941 903 1339 934"> <small>x9,000 10.0kV LED SEM WD 9mm 12:11:36 1µm UM-EMAL 2020-02-04</small> </p>
<p>290841-3</p>		

## Additional References not cited in the Main Text

- Andrade, C.A., and Barton, E.D., 2005, The Guajira upwelling system: Continental Shelf Research, v. 25, p. 1003–1022, doi:[10.1016/j.csr.2004.12.012](https://doi.org/10.1016/j.csr.2004.12.012).
- Gates, R.D., 1990, Seawater temperature and sublethal coral bleaching in Jamaica: Coral Reefs, v. 8, p. 193–197, doi:10.1007/BF00265010.
- Harris, I., Jones, P.D., Osborn, T.J., and Lister, D.H., 2014, Updated high-resolution grids of monthly climatic observations - the CRU TS3.10 Dataset: Journal of Climatology, v. 34, p. 623–642, doi:[10.1002/joc.3711](https://doi.org/10.1002/joc.3711).
- Huang, B., Thorne, P.W., Banzon, V.F., Boyer, T., Chepurin, G., Lawrimore, J.H., Menne, M.J., Smith, T.M., Vose, R.S. and Zhang, H., 2017, NOAA Extended Reconstructed Sea Surface Temperature (ERSST), Version 5. 1930-2016. NOAA National Centers for Environmental Information. doi:10.7289/V5T72FNM.
- IAEA/WMO, 2018, Global Network of Isotopes in Precipitation: The GNIP Database, Accessible at: <https://nucleus.iaea.org/wiser>
- Johnson E.H., Anderson, B.M., and Allmon, W.D., 2017, What can we learn from all those pieces? Obtaining data on drilling predation from fragmented high-spired gastropod shells, *Palaios* v. 32, p. 271-277. doi: [10.2110/palo.2016.088](https://doi.org/10.2110/palo.2016.088)
- Jury, M.R., 2018, Eastern Venezuela coastal upwelling in context of regional weather and climate variability: Regional Studies in Marine Science, v. 18, p. 219–228, doi:[10.1016/j.rsma.2017.10.010](https://doi.org/10.1016/j.rsma.2017.10.010).
- Montoya-Sánchez, R.A., Devis-Morales, A., Bernal, G., and Poveda, G., 2018, Seasonal and intraseasonal variability of active and quiescent upwelling events in the Guajira system, southern Caribbean Sea: Continental Shelf Research, v. 171, p. 97–112, doi:[10.1016/j.csr.2018.10.006](https://doi.org/10.1016/j.csr.2018.10.006).
- Moreno-Díaz, G., Rojas-Herrera, A.A., Violante-González, J., González-González, J., Acevedo, J.L.R., and Ibáñez, S.G., 2015, Temporal Variation in Composition and Abundance of Phytoplankton Species during 2011 and 2012 in Acapulco Bay, Mexico: Open Journal of Marine Science, v. 05, p. 358–367, doi:10.4236/ojms.2015.53029.
- Rojas-Herrera, A.A., Violante-González, J., García-Ibáñez, S., Villerías-Salinas, S., and Moreno-Díaz, G., 2016, Temporal Variation of the Pelagic Copepod Community in Acapulco Bay, Mexico: Open Journal of Marine Science, v. 06, p. 40–48, doi:10.4236/ojms.2016.61005.

## **A modern calibration for the reconstruction of seasonal precipitation patterns from isotope sclerochronology of coastal turritellid gastropods**

### **Abstract:**

Turritellid gastropods are aragonitic marine mollusks that are particularly abundant and widespread in the fossil record. With fast growth rates and a shallow coastal living environment, they have the potential to be excellent recorders of ancient subannual climate variation – both seasonal temperature changes and fluctuations in coastal  $\delta^{18}\text{O}_{\text{sw}}$ . Changes in coastal  $\delta^{18}\text{O}_{\text{sw}}$  can be driven by seasonally variable freshwater delivery, related to local rainfall patterns. We produce 18 new high-resolution oxygen isotope profiles of modern turritellid shells, and compare these and other published records to instrumental temperature and precipitation data to assess the potential of turritellids to record past sea surface temperatures and seasonal precipitation patterns. We find that the annual range in shell  $\delta^{18}\text{O}$  is related to seasonal precipitation variance (SPV) once seasonal changes in sea surface temperature (SST) are accounted for. We also demonstrate the effects of alignment vs. misalignment of precipitation and temperature maxima on  $\delta^{18}\text{O}$  profiles using synthetic data. We produce an empirical relationship between  $\delta^{18}\text{O}_{\text{range}}$ , SST and SPV can be used to reconstruct paleoenvironmental conditions, particularly in the tropics where seasonal precipitation has a strong effect on  $\delta^{18}\text{O}$ .

### **Introduction:**

Seasonality is an important component of climate variability, yet it is difficult to reconstruct deep in the geologic past due to time-averaging in many paleoclimate archive materials. Seasonal temperature cycles and precipitation patterns are particularly important constraints on the distribution of flora and fauna, as biota are more sensitive to seasonal extremes than to average climate parameters such as mean annual temperature (MAT) or mean annual precipitation (MAP). Understanding how the seasonal cycle of precipitation will change in a warming world is challenging, as coupled climate models show poor skill in this area (Joetzer et al., 2013). Paleoclimate data that resolve seasonal precipitation can provide insight into how SPV has been impacted by past mean state changes. However, paleoprecipitation records remain somewhat elusive, due to the lack of appropriate paleoclimate archive materials.

Turritellid gastropods (genus *Turritella*, family Turritellidae) are extremely abundant and widespread in the fossil record, occurring on all continents and in nearly every marine deposit since the early Cretaceous (Allmon, 2011). They live primarily in shallow coastal waters, and grow rapidly during their juvenile stage. Many previous isotope-based paleoclimate studies have focused on bivalves instead of gastropods due to their longevity, but their typically slower growth rates result in annual growth bands that are often 1mm in width or less (e.g. Buick and Ivany, 2004; Schoene et al., 2005). This means that micro-drilling is required to sample material at a sub-yearly scale. In contrast, turritellids are particularly fast growing, with the largest species depositing upwards of 35g of carbonate in the first year of life (Anderson and Allmon, 2020). This means that routine sampling methods using a hand-held drill can extract many data points

per season, easily creating a high-resolution subannual record of climate (e.g. Scholz et al., 2020). The rapid growth rate also allows for the collection of larger quantities of carbonate powder while maintaining sub-annual resolution – an important feature necessary for certain techniques that require more material, such as clumped isotope paleothermometry.

Turritellid shells have previously been used for stable isotope-based paleoenvironment and paleoseasonality reconstructions, and the sinusoidal nature of turritellid  $\delta^{18}\text{O}$  profiles (as seen in Figure 1) suggest that they can be excellent recorders of paleoseasonality, without the significant seasonal biases due to stoppages of growth seen in other taxa (e.g. Surge et al., 2001). The  $\delta^{18}\text{O}$  of shell carbonate is controlled by two factors: the temperature, and isotopic composition of the water the shell grew in (seawater for marine taxa,  $\delta^{18}\text{O}_{\text{sw}}$ ) (Kim et al., 2007; Grossman and Ku, 1986). Allmon (1992) found that the subannual range in  $\delta^{18}\text{O}$

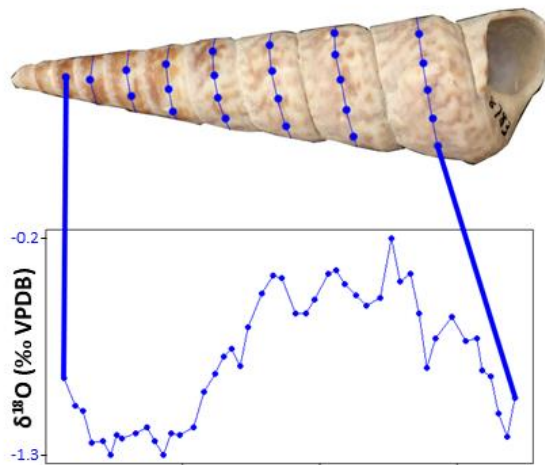


Figure 1. Modern turritellid (*T. variegata*, sample Var-Col-B) showing sampling scheme and sinusoidal  $\delta^{18}\text{O}$  profile.

from a modern specimen of *T. gonostoma* collected in the Gulf of California accurately reconstructed the annual sea surface temperature (SST) range when  $\delta^{18}\text{O}_{\text{sw}}$  was assumed fixed. Andreasson & Schmitz (1996, 1998, 2000) used turritellid  $\delta^{18}\text{O}$  profiles to reconstruct annual SST ranges during the early middle Eocene, again assuming  $\delta^{18}\text{O}_{\text{sw}}$  was constant throughout the year, and Jones & Allmon (1999) used a similar approach on Pliocene-age turritellids. However, the assumption that the isotopic composition of seawater was constant throughout the year could have biased their estimates of SST seasonality. In reality,  $\delta^{18}\text{O}_{\text{sw}}$  can vary quite significantly on a subannual scale, especially in the coastal and marginal marine environments where turritellids live. This variation could be due to seasonally variable freshwater precipitation and discharge (e.g. Dettman et al., 2004), or the advection of water masses from different areas, depending on the location. This makes interpreting turritellid  $\delta^{18}\text{O}$  profiles complicated, as it can be difficult to parse if the shells are recording seasonal temperature variations,  $\delta^{18}\text{O}_{\text{sw}}$  changes, or a combination of the two (Tao et al., 2013).

In order to accurately use turritellid oxygen isotope profiles to reconstruct paleoseasonality, it is essential to validate how turritellids record seasonal climate cycles in a modern context, where detailed instrumental climate data exists for comparison. Here, we produce subannual isotope profiles from shells of modern turritellids, sourced from a variety of latitudes and species, in order to study relationships between both average and subannual  $\delta^{18}\text{O}_{\text{carb}}$  values and instrumental climate parameters including temperature, precipitation, and  $\delta^{18}\text{O}_{\text{sw}}$ . We also generate synthetic  $\delta^{18}\text{O}$  profiles, which show that seasonal temperature and precipitation can constructively or destructively interfere in the resulting  $\delta^{18}\text{O}$  signal, leading to over- or underestimations of seasonal temperature ranges depending on whether the maximum precipitation coincides with the warmest season or not. Traditional sclerochronological studies



do not consider the variations in  $\delta^{18}\text{O}_{\text{sw}}$  or this seasonal interference, both of which may be significantly biasing their results.

### Methods:

Sixteen turrnellid shells representing six different species (*T. variegata*, *T. gonostoma*, *T. terebra*, *T. leucostoma*, *T. carinifera* and *T. rosea*) were obtained from the University of Michigan Zoology Collections. These shells were collected from 9 locations worldwide: Venezuela, Jamaica, Mexico, Costa Rica, the Philippines, South Africa, Australia, and England (red stars, Figure 2). Two more turrnellids were collected from the Guajira Peninsula, Colombia (*T. variegata*, yellow box, Figure 2) as part of a previous study (Scholz et al., 2020), for a total of eighteen modern shell samples. Using a handheld drill set to the lowest possible speed (1000 rpm), shells were sampled at a subannual scale along the spiral growth direction (Figure 1). Accumulated distance (in mm) was recorded starting at 0 near the apex, and increasing along the spiral direction towards the aperture. Each sample was taken from the middle of the whorl, equidistant from each side. 12-47 samples were taken per shell, depending on shell size, with most shells having 20-30 samples. Carbonate powders were analyzed for  $\delta^{13}\text{C}$  and  $\delta^{18}\text{O}$  using a Kiel IV device attached to a Thermo-MAT 253 mass spectrometer and were calibrated against NBS-19 and NBS-18, run daily. Analytical error was better than  $\pm 0.1\%$  for both  $\delta^{13}\text{C}$  and  $\delta^{18}\text{O}$ . All  $\delta^{13}\text{C}$  and  $\delta^{18}\text{O}$  data are presented relative to Vienna Pee Dee Belemnite (VPDB).



Figure 2. Map showing all collection localities. Color and symbol based on sample source. Red star = University of Michigan Zoology Collections, yellow square = collected by collaborator on Guajira Peninsula, Colombia, green circle = previously published in Allmon 1992, 1994.

In addition to these eighteen samples, published data from five additional shells (green circles, Figure 1; Allmon, 1992; 1994) was included to expand our dataset – three from Puerto Penasco, Mexico (*T. gonostoma*), and two from Hobart, Tasmania (closely related genus *M. roseus*). Minimum and maximum  $\delta^{18}\text{O}$  for each of these five shells was determined from figures in the original papers, but average and median  $\delta^{18}\text{O}$  values for these shells could not be accurately reported due to lack of access to raw data.

Monthly average sea surface temperature (SST) data for each sample location was calculated from NOAA ERSST v.5 (Huang et al., 2017), which has temperatures derived from the International Comprehensive Ocean–Atmosphere Dataset. Monthly average precipitation data was calculated from the CRU 3.25 Global Precipitation dataset (Harris et al., 2014). For both SST and precipitation, monthly data was averaged over the period 1980–2012 for a rectangular spatial region ( $2^\circ \times 2^\circ$ ) around the sample location (Table S1). The annual range in SST was determined as the difference between the minimum and maximum monthly mean values. Mean annual sea surface temperature (MASST) was determined by taking the average of all monthly means. Mean annual precipitation (MAP) was calculated by summing the monthly means and seasonal precipitation variance was calculated by taking the difference between the highest and lowest (rainiest and driest) individual months.

Using these instrumental monthly temperature and precipitation values, smoothed annual patterns for temperature and precipitation were modeled with a fourth order harmonic in the form

$$T, P = k_1 \sin\left(\frac{2\omega_1\pi}{12m}\right) + k_2 \cos\left(\frac{2\omega_2\pi}{12m}\right) + k_3 \sin\left(\frac{4\omega_3\pi}{12m}\right) + k_4 \cos\left(\frac{4\omega_4\pi}{12m}\right)$$

where  $k$  and  $\omega$  are coefficients, and  $m$  is the month (an integer 1–12). This resulted in modeled monthly temperature ( $T$ ) and precipitation ( $P$ ) profiles for each site (Figure 3), which were later used in the creation of synthetic annual  $\delta^{18}\text{O}$  profiles.

### Results:

$\delta^{18}\text{O}$  values for all shells ranged from  $-2.38\text{‰}$  to  $+2.36\text{‰}$ . Within a single shell, the  $\delta^{18}\text{O}$  range (minimum to maximum  $\delta^{18}\text{O}$  value) varied from  $0.63\text{‰}$  to  $2.75\text{‰}$  (Figure 4a).  $\delta^{13}\text{C}$  values ranged from  $+0.12\text{‰}$  to  $+3.83\text{‰}$  across all individual points, with individual shell ranges varying from  $0.6\text{‰}$  to  $2.17\text{‰}$  (Figure 4b).  $\delta^{18}\text{O}$  profiles were mostly sinusoidal in nature, showing alternating peaks and troughs, indicating the full seasonal range in conditions was likely being captured by this sampling resolution. An exception to this was the sample Ros-Australia-2, which showed sharper peaks than seen in other samples, potentially indicating seasonal aliasing (growth slowdown/stoppage) at the higher  $\delta^{18}\text{O}$  end. Another sample (Leu-Mexico) also showed slightly sharper peaks.  $\delta^{13}\text{C}$  profiles showed less coherent subannual/seasonal variations, though

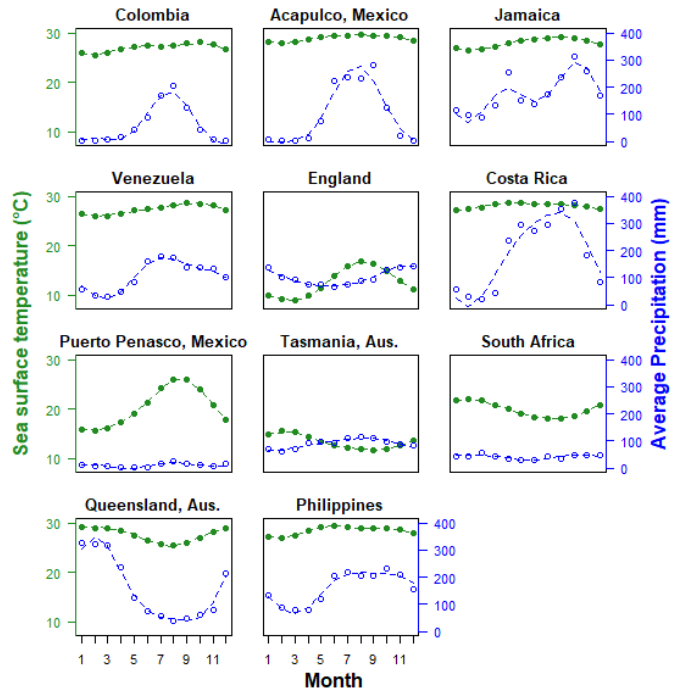


Figure 3. Temperature and precipitation data (points) and modeled seasonal regime (dashed line) for all sites.



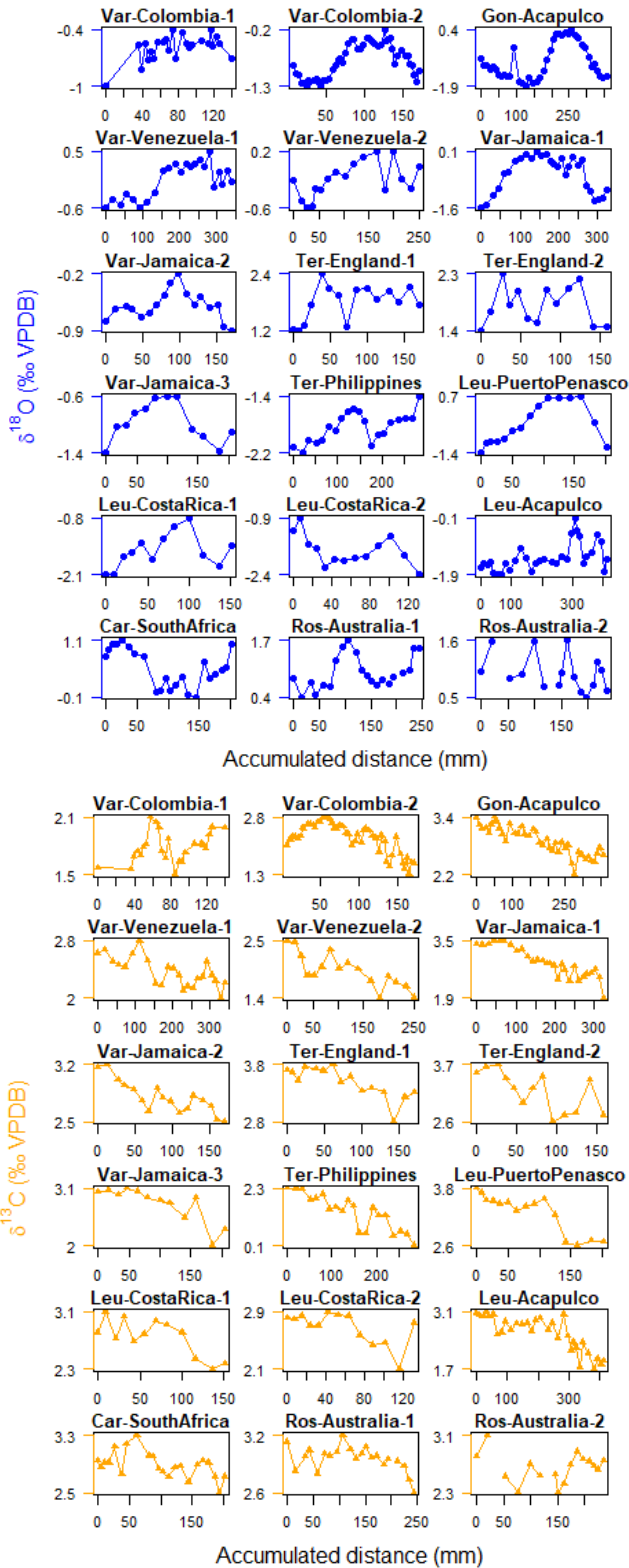


Figure 4a and 4b.  $\delta^{18}\text{O}$  (top, blue) and  $\delta^{13}\text{C}$  (bottom, orange) profiles for all shells. Minimum and maximum isotopic values for each shell are shown on the y-axis and vary for each shell. Sample naming scheme: Species-Location-Number.

most samples did tend to decrease in  $\delta^{13}\text{C}$  throughout their lifetime, with the exception of Var-Colombia-1 and Var-Colombia-2. Figure S1 shows the correlation between  $\delta^{18}\text{O}$  and  $\delta^{13}\text{C}$  for each shell.

Temperature and precipitation regimes, as recorded by instrumental data, were also variable between the 11 sites (Figure 3). Annual SST ranges were lowest in the tropical locations, with the smallest annual range ( $1.6^\circ\text{C}$ ) in Costa Rica. The highest annual SST range ( $10.4^\circ\text{C}$ ) was recorded in Puerto Penasco, Mexico, likely due to the Gulf of California's unique seasonal gyre (Lavin et al., 2014). MASSTs varied from a low of  $12.6^\circ\text{C}$  in England to a high of  $28.9^\circ\text{C}$  in Acapulco, Mexico. Precipitation regimes also varied greatly between sites, with Puerto Penasco experiencing as little as 23 mm difference between the wettest and driest months, while Costa Rica experiencing much higher (355 mm) variation between wet and dry months. MAPs varied from a low of 116 mm/yr in Puerto Penasco, Mexico to a high of 2242 mm/yr in Costa Rica.

## Discussion:

In previous studies (e.g. Allmon 1992; Andreasson & Schmitz 1996, 1998, 2000; Jones & Allmon 1999), subannual profiles of carbonate  $\delta^{18}\text{O}$  were converted directly into subannual temperature records, assuming  $\delta^{18}\text{O}_{\text{sw}}$  was invariant. However, given the shallow coastal habitat of turrnellids, often living in waters less than 5m deep (Allmon, 2011), this assumption of invariant  $\delta^{18}\text{O}_{\text{sw}}$  is flawed. To see if our samples accurately recorded seasonal temperatures using this method, we calculated the seasonal temperature range in each of our samples assuming an

invariant  $\delta^{18}\text{O}_{\text{sw}}$ . This was done using the relationship presented in Kim et al., 2007 for synthetic aragonite, which we linearized as follows:

$$\delta^{18}\text{O} = 3.63 - 0.21(T) + \delta^{18}\text{O}_{\text{sw}} \quad (1)$$

For each shell, minimum and maximum temperatures were calculated using the maximum and minimum  $\delta^{18}\text{O}$  values, and an invariant  $\delta^{18}\text{O}_{\text{sw}}$ . The difference between these two values was taken as the seasonal range in temperature. Figure 5 shows the results of the calculated temperatures, compared to the instrumental SST ranges.

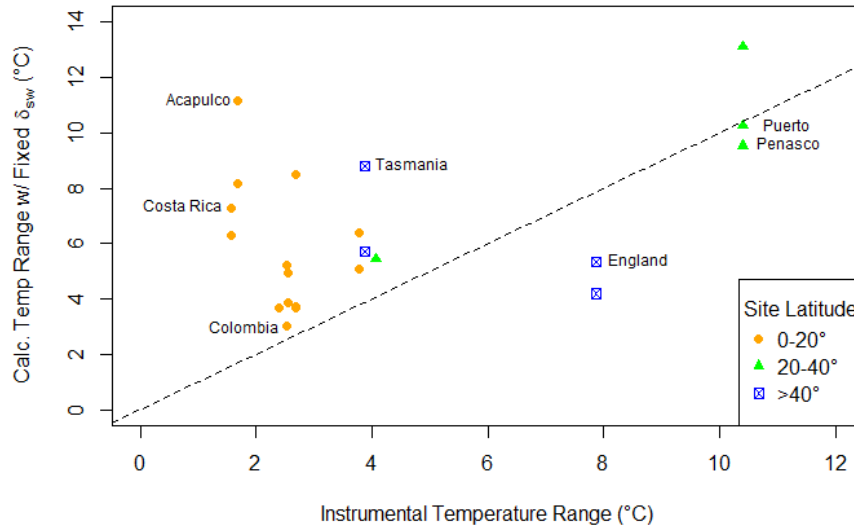


Figure 5. Calculated temperature ranges from  $\delta^{18}\text{O}$  data, compared with the instrumental seasonal temperature ranges. Dashed line is the 1:1 line. Most points, especially the tropical locations, overestimate the seasonal temperature range significantly. Only the shells from England underestimate the range.

Most of our samples significantly overestimate the seasonal temperature range, particularly the samples from the tropics. The farthest outlier is a shell from Acapulco, Mexico which has a  $\delta^{18}\text{O}$  range that translates into a seasonal temperature range of 11.1°C, almost 10°C higher than the instrumental value of 1.7°C. In contrast, the shells from England suggest seasonal temperature ranges of 4.2 and 5.3°C, compared to the true value of 7.8°C, underestimating the temperature seasonality by 3–4°C. The scale of these discrepancies show that these shells are not simply recording temperature range, but that they are likely influenced by substantial seasonal  $\delta^{18}\text{O}_{\text{sw}}$  variations.

$\delta^{18}\text{O}_{\text{sw}}$  of coastal waters can easily vary throughout the year due to seasonally-variable precipitation and surface runoff from nearby continents. Here we attempt to disentangle the competing influences of changes in temperature and changes in  $\delta^{18}\text{O}_{\text{sw}}$  on the resulting carbonate  $\delta^{18}\text{O}$  profiles.

### ***I. Median $\delta^{18}\text{O}_{\text{carb}}$ values and average climate parameters***

To determine what climate parameters the turrnellids are truly recording, we first examined whether the median  $\delta^{18}\text{O}$  values from each shell accurately represented local average temperature and  $\delta^{18}\text{O}_{\text{sw}}$  values. The median  $\delta^{18}\text{O}$  value was used instead of the mean, in an attempt to make sure the analysis was not skewed towards single-point seasonal extremes but rather represented the most common temperature and  $\delta^{18}\text{O}_{\text{sw}}$  experienced by the organism throughout the year (see Figure S2 for mean  $\delta^{18}\text{O}$  results, which were not significantly different

from median  $\delta^{18}\text{O}$ ). Figure 6a shows the median  $\delta^{18}\text{O}$  of each shell plotted against the MASST at each site. The observed negative correlation matches the relationship expected from laboratory studies of synthetic and biogenic carbonates (Kim et al., 2007; Grossman & Ku, 1986), but significant spread is present amongst the tropical sites. Despite this spread, a basic linear regression yields:

$$\text{Median } \delta^{18}\text{O} = (3.92 \pm 0.66) - (0.18 \pm 0.03)\text{MASST} \quad (2)$$

The regression has a slope of  $-0.18 \pm 0.03$  and an intercept of  $3.92 \pm 0.66$  (1 standard error, 1 SE). These coefficients are very similar to the established relationship for synthetic aragonite presented by Kim et al. (2007) (black line, Figure 6a).

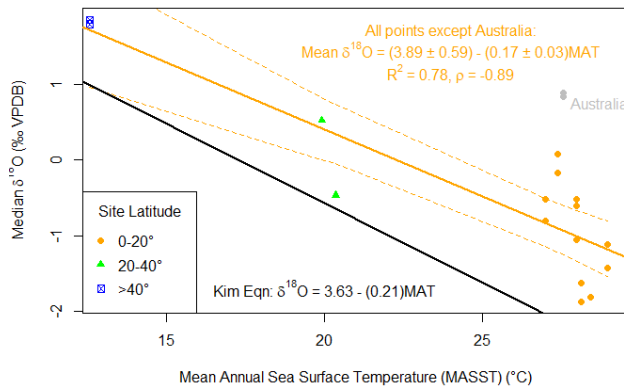


Figure 6a. Median  $\delta^{18}\text{O}$  of all shells plotted against MASST. Coefficients of the linear regression (orange) are similar to those found in Kim et al., 2007 (black). Dashed lines show 95% confidence interval of the model.

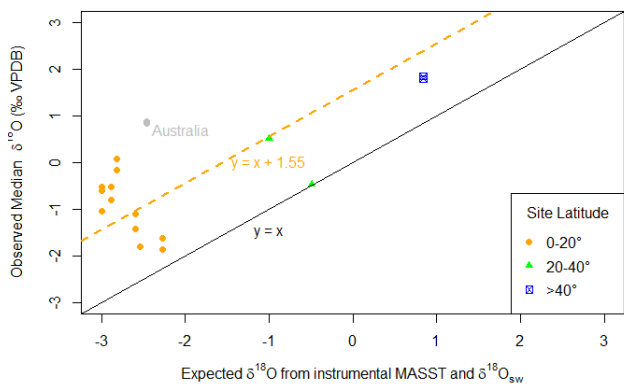


Figure 6b. Observed median  $\delta^{18}\text{O}$  plotted against the expected  $\delta^{18}\text{O}$ , given MASST and  $\delta^{18}\text{O}_{\text{sw}}$  values from LeGrande et al., 2006. Our samples are vertically offset from the 1:1 line by +1.55‰.

Across latitudes, median  $\delta^{18}\text{O}$  and MASST are fairly well correlated ( $R^2 = 0.75$ , Pearson correlation coefficient ( $\rho$ ) = -0.88,  $p$  value =  $8\text{E}-6$ ). However, variance in the tropics, the region which was most thoroughly sampled, shows that significant local variations exist as well. Two samples from the Torres Strait, Australia, are particularly different from expected (in these and other figures), with a very high median  $\delta^{18}\text{O}$  relative to the high MASST, potentially indicative of unusual  $\delta^{18}\text{O}_{\text{sw}}$  conditions. These samples were excluded from this regression as outliers, but will be discussed in more detail below.

Figure 6a shows that our samples are uniformly higher in  $\delta^{18}\text{O}$  than expected, given the equation from Kim et al., 2007. To determine if this was due to varying  $\delta^{18}\text{O}_{\text{sw}}$  values or a potential vital effect of turrillids, we obtained average  $\delta^{18}\text{O}_{\text{sw}}$  values from all locations from LeGrande et al., 2006, a gridded interpolation based on data from the Global Seawater Oxygen-18 Database from NASA GISS (Schmidt et al., 1999). Using these  $\delta^{18}\text{O}_{\text{sw}}$  values and the instrumental MASST, we calculated the expected average  $\delta^{18}\text{O}$  for each site according to the Kim et al. (2007) equation:

$$\text{Expected } \delta^{18}\text{O} = 3.63 - (0.21)\text{MASST} + \delta^{18}\text{O}_{\text{sw-GISS}} \quad (3)$$

Figure 6b shows the observed median  $\delta^{18}\text{O}$  plotted against the expected average  $\delta^{18}\text{O}$  value from these instrumental measurements. All our samples plot above the 1:1 line, with an average offset of +1.55‰ above the expected value (calculated by performing a linear regression with the slope held constant at one). This offset could be the result of a vital effect in turrnellids, or a cold-seasonal bias in their growth patterns, though neither have been recorded previously. The seasonal bias explanation is not supported by the sinusoidal structure of the  $\delta^{18}\text{O}$  profiles (Figure 3), which would show sharper peaks if the shells stopped growth during certain seasons (e.g. Surge et al., 2001; Ivany 2012). The only samples that show sharp peaks potentially indicating seasonally biased profiles are those from Australia (particularly Ros-Australia-2), which may be why they plot as outliers in Figure 6a and 6b. This may be a species-specific effect, but it cannot be determined in this study as there are no other *T. rosea* samples in our sample set to compare to. However, since these samples were purposefully excluded from the above regressions, they do not affect the calculated offset. The remaining samples combine to show this 1.55‰ positive offset, while having sinusoidal  $\delta^{18}\text{O}$  profiles indicating year-round growth, making it more likely that this offset is a vital effect of turrnellids in general.

The other possibility is that the LeGrande  $\delta^{18}\text{O}_{\text{sw}}$  values are around 1.5‰ lighter than the values that are truly occurring in shallow coastal habitats, either due to modeling methods or due to spatial incompleteness in the source dataset. However, coastal regions are expected to be, if anything, more isotopically depleted in  $\delta^{18}\text{O}_{\text{sw}}$  relative to open ocean seawater due to concentrated freshwater runoff (see below). Freshwater delivery to coastal regions would deplete coastal waters relative to the open ocean, so it is far more likely that the LeGrande model predicts  $\delta^{18}\text{O}_{\text{sw}}$  that are heavier than actual coastal values, as most of the source data was collected in the open ocean. If coastal waters were actually more depleted in  $\delta^{18}\text{O}_{\text{sw}}$  than the open ocean values used in Figure 6b, we would expect real data points to fall below, not above, the 1:1 line. We therefore suggest that turrnellids fractionate oxygen isotopes slightly out of equilibrium with the surrounding water, with a positive offset of ~1.5‰, but simultaneous collection and isotopic analysis of inhabited seawater alongside living shells is needed to confirm this.

## ***II. Subannual $\delta^{18}\text{O}$ ranges and subannual climate parameters***

A vital effect of this nature (a fixed offset) or incorrect  $\delta^{18}\text{O}_{\text{sw}}$  from the GISS database will affect the calculated median  $\delta^{18}\text{O}$  values in each shell, but it would not likely affect the subannual range seen in individual specimens. To investigate the ability of turrnellids to capture subannual climatology, subannual ranges in  $\delta^{18}\text{O}$  were compared with annual SST range and seasonal precipitation variance. Figure 7 shows a slight positive relationship between range in  $\delta^{18}\text{O}$  and range in SST, with an  $R^2$  of 0.21 and Pearson correlation coefficient  $\rho = 0.49$ , but tropical localities show a large spread in  $\delta^{18}\text{O}$  range (0.63 to 2.34‰) despite spanning annual SST ranges of only 1-4°C. Figure 8 shows the range in  $\delta^{18}\text{O}$  of each shell plotted against seasonal precipitation variance at each site. No significant correlation is seen when all localities are combined ( $R^2$  of 0.01). However, tropical localities taken separately show a positive relationship (increasing range in  $\delta^{18}\text{O}$  with increasing precipitation variance) with an  $R^2$  of 0.25 and  $\rho = 0.53$ . This behavior is in line with expectations, which would predict that tropical locations with limited variation in SST would be more strongly influenced by seasonally variable precipitation

via  $\delta^{18}\text{O}_{\text{sw}}$  changes, whereas higher latitude sites with larger seasonality in SST would show a stronger relationship with SST range than with precipitation variance.

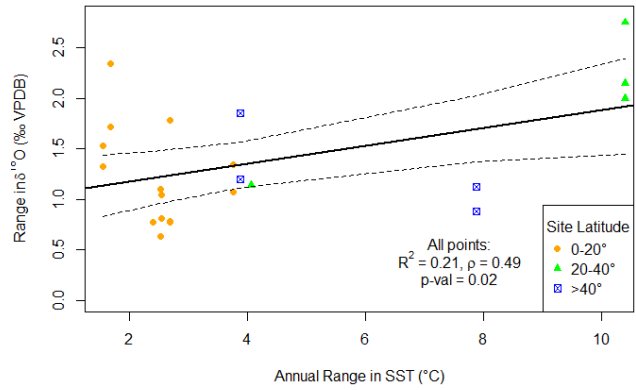


Figure 7. Range in  $\delta^{18}\text{O}$  (maximum to minimum) for each shell plotted against annual range in SST. Black shows linear regression, dashed lines are 95% confidence intervals.

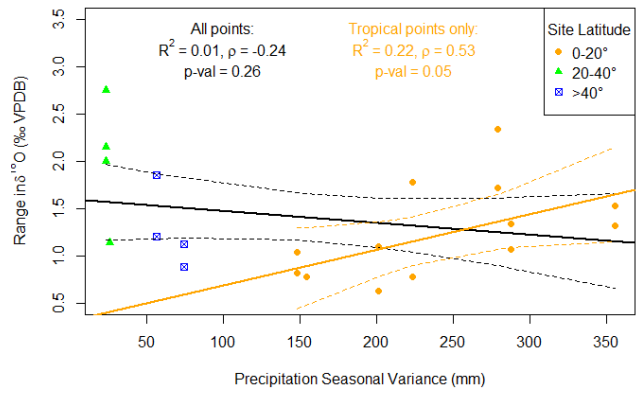


Figure 8. Range in  $\delta^{18}\text{O}$  for each shell plotted against seasonal variance in precipitation. No correlation overall, though tropical points show a slight positive correlation.

Overall, range in  $\delta^{18}\text{O}$  seen in each shell does not correlate very strongly with either the SST range or the precipitation variance alone. We suggest that this is due to the combined effects of temperature and  $\delta^{18}\text{O}_{\text{sw}}$  (representing precipitation variance) on carbonate  $\delta^{18}\text{O}$ , which can interact either constructively or destructively to amplify or damp the  $\delta^{18}\text{O}$  signal in the shell carbonate ( $\delta^{18}\text{O}_{\text{carb}}$ ), depending on the seasonal pattern at individual sites. If maximum precipitation (leading to most negative  $\delta^{18}\text{O}_{\text{sw}}$  values) aligns with the warmest season, the effects will be additive. If the season of maximum precipitation does not align with the warmest season, the two parameters would have opposing effects on the  $\delta^{18}\text{O}_{\text{carb}}$ , effectively damping the signals from both temperature and  $\delta^{18}\text{O}_{\text{sw}}$  changes.

### III. Removing the SST signal

To separate these competing effects, we estimate the amount of influence that annual SST change should have on the range in  $\delta^{18}\text{O}_{\text{carb}}$ . Using the instrumental range in SST determined for each site, we calculated the SST equivalent in carbonate  $\delta^{18}\text{O}$ : the range in carbonate  $\delta^{18}\text{O}$  expected if only controlled by the seasonal temperature change (i.e. assuming no changes in  $\delta^{18}\text{O}_{\text{sw}}$ ). This was calculated as follows:

$$\delta^{18}\text{O}_{\text{SST eq.}} = 0.21 * \Delta\text{SST} \quad (4)$$

where the coefficient of 0.21 is the experimentally derived relationship between aragonite  $\delta^{18}\text{O}$  and temperature found by Kim et al. (2007). This SST equivalent in  $\delta^{18}\text{O}_{\text{carb}}$  was then subtracted from the observed range in  $\delta^{18}\text{O}_{\text{carb}}$  in each shell to show how much  $\delta^{18}\text{O}$  variation remains, presumably caused by seasonal changes in  $\delta^{18}\text{O}_{\text{sw}}$ .

$$\text{apparent range in } \delta^{18}\text{O}_{\text{sw}} = \delta^{18}\text{O}_{\text{range observed}} - \delta^{18}\text{O}_{\text{SST eq.}} \quad (5)$$

We call the resulting value the apparent range in  $\delta^{18}\text{O}_{\text{sw}}$ . This calculation assumes that temperature and  $\delta^{18}\text{O}_{\text{sw}}$  are varying in-phase, or additively, with each other, which is not uniformly true (see Figure 4). However, in areas where peak precipitation aligns with the warmest months and/or where the seasonal range in SST is very small, it provides a workable approximation.

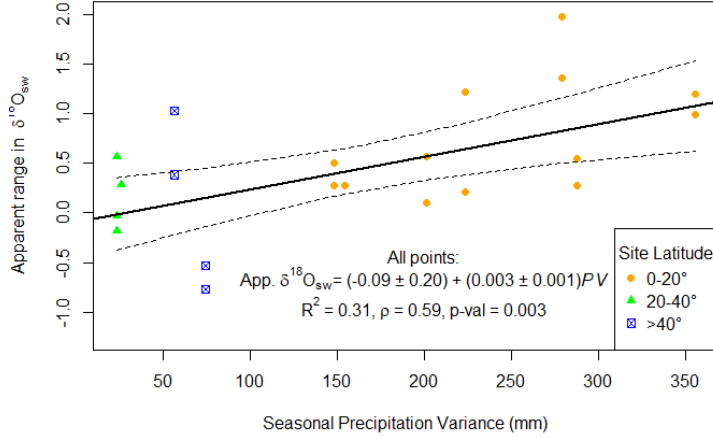


Figure 9: Relationship between precipitation variance and the apparent range in  $\delta^{18}\text{O}_{\text{sw}}$ , calculated as the observed  $\delta^{18}\text{O}$  range minus the SST equivalent in  $\delta^{18}\text{O}$ . PV = Precipitation variance. Dashed line shows 95% confidence interval of the model.

Figure 9 shows the relationship between the calculated apparent range in  $\delta^{18}\text{O}_{\text{sw}}$  and the seasonal variance of precipitation (SPV). The relationship was quantified as follows, and solved for SPV:

$$\text{Apparent range in } \delta^{18}\text{O}_{\text{sw}} = (-0.09 \pm 0.20) + (0.003 \pm 0.001)\text{SPV} \quad (6a)$$

$$\text{SPV} = (329 \pm 99) * \text{Apparent range in } \delta^{18}\text{O}_{\text{sw}} + (27.4 \pm 61) \quad (6b)$$

$$\text{SPV} = (329 \pm 99) * (\delta^{18}\text{O}_{\text{range}} - 0.21 * \Delta\text{SST}) + (27.4 \pm 61) \quad (6c)$$

The correlation is improved over the relationship in Figure 8, where precipitation variance is plotted against the raw  $\delta^{18}\text{O}$  range. In particular, higher latitude sites with larger SST ranges are brought into alignment with tropical sites, which already showed a significant correlation with SPV.

Although the uncertainties in this relationship are significant, in terms of reconstructing past precipitation variance, the relationship is strong enough that it can still give an indication of the type of precipitation regime at the paleo-location. The large seasonal variance in a location like Costa Rica, which has a tropical monsoonal climate with a variance of 355mm each year, is easily distinguishable from the very small variance of 23mm/year in a hot desert climate like Puerto Penasco, Mexico. This information could therefore be used to infer climate information such as the Koppen climate zone of the location, which is often based on precipitation amount and variance, among other factors (See discussion in supplement; Figure S3).

The qualitative relationship between apparent  $\delta^{18}\text{O}_{\text{sw}}$  and SPV observed from a subset of data shown in Figure 9 was used to conclude that the Guajira Peninsula, Colombia experienced increased precipitation variance during the Miocene (Scholz et al., 2020). This conclusion was supported by the presence of fossils of wet-loving flora and fauna not present in the region today. If we instead use equation 6 and the elevated range in  $\delta^{18}\text{O}$  seen in fossil shells from this site (on average 1.4‰), we would estimate 313 mm/yr of seasonal variance, more than 100mm higher



than the modern value of 201mm/yr, and consistent with the geologic evidence that suggests a fluvio-deltaic environment with year-round lakes (Moreno et al., 2015) and fauna such as turtles and fish tolerant of reduced salinity conditions (Hendy et al., 2015; Carrillo et al., 2018). However, the error on this calculation is substantial, with a worst-case estimate of  $\pm 147$  mm/yr due to the high errors on the slope and intercept. These high uncertainty estimates are due to the noise and variance within the dataset, which are likely due to a variety of site-specific factors. When the same relationship is modeled synthetically (Section VI), there is significantly lower uncertainty despite the coefficients of the relationship being nearly identical, suggesting that this calculation is potentially more robust than these initial uncertainties suggest.

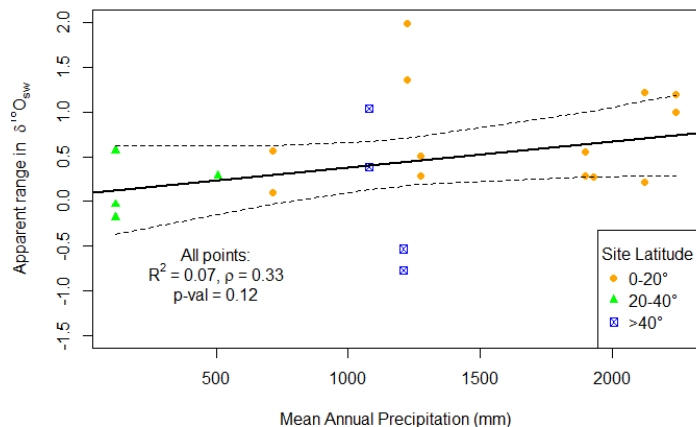


Figure 10: Relationship between mean annual precipitation (MAP) and the apparent range in  $\delta^{18}\text{O}_{\text{sw}}$ , calculated as the observed  $\delta^{18}\text{O}$  range minus the SST equivalent in  $\delta^{18}\text{O}$ . No significant trend.

In contrast to the above relationship between apparent  $\delta^{18}\text{O}_{\text{sw}}$  and seasonal variance of precipitation, total annual rainfall (MAP) showed a much weaker relationship with the apparent  $\delta^{18}\text{O}_{\text{sw}}$  (Figure 10), or with the raw  $\delta^{18}\text{O}$  ranges (Figure S4). We argue this is because while locations with a higher MAP may have lower coastal  $\delta^{18}\text{O}_{\text{sw}}$  values on average year-round, this does not affect the seasonal variation in  $\delta^{18}\text{O}_{\text{sw}}$ , only the average  $\delta^{18}\text{O}_{\text{sw}}$  value. In contrast, seasonal variations in the amount of precipitation would change the volume of isotopically depleted surface runoff added to coastal waters, creating subannual changes in  $\delta^{18}\text{O}_{\text{sw}}$ .

#### IV. Examining Seasonal Lag

The ‘apparent  $\delta^{18}\text{O}_{\text{sw}}$ ’ approach does not take into account the interactions with seasonal lag between temperature and precipitation maxima. The calculation of apparent range in  $\delta^{18}\text{O}_{\text{sw}}$  (Eqn 5) assumes that changes in  $\delta^{18}\text{O}_{\text{sw}}$  (via precipitation) and SST are correlated. However, in many sites this is not the case. For example, if maximum rainfall occurs in winter when temperatures are lowest, the resulting range in  $\delta^{18}\text{O}$  will be smaller and the range in apparent  $\delta^{18}\text{O}_{\text{sw}}$  may even be negative. Therefore, the phasing of seasonal cycles may be an important factor to consider when modeling these relationships, as it might artificially damp estimates of past annual SST range.

To this end, the amount of ‘seasonal lag’ between the season of highest precipitation and the warmest season was determined for each site, as follows. For each three-month season (DJF, MAM, JJA, SON), the average temperature was calculated, along with the sum of the rainfall in those three months. If the warmest season coincides with the season of highest precipitation, the seasonal lag is defined as 0. If the season of highest precipitation is one off in either direction from the warmest month (e.g. most rainfall in MAM or SON, warmest temperatures in JJA), the



seasonal lag is defined as 1. If the seasons are opposite (e.g. warmest in JJA, most rainfall in DJF), the seasonal lag is defined as 2. Figure 11 shows the points colored according to their seasonal lag classification, alongside the linear model defined in equation 6.

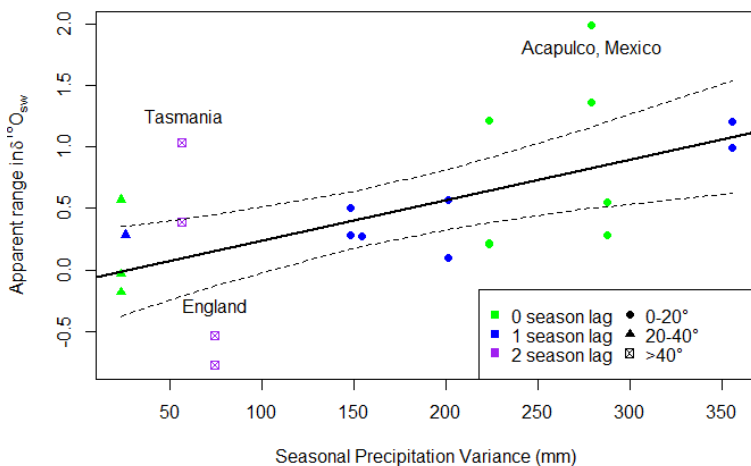


Figure 11: Points colored by amount of seasonal lag. Line shows the linear model described in equation 6 with 95% confidence intervals.

Shells from locations with a seasonal lag of 2 (England, Tasmania) are some of the furthest away from the model, potentially due to damping effects of the opposing signals of precipitation and temperature. The farthest outlier, however, is a shell from Acapulco, Mexico, with a seasonal lag of zero. The Acapulco shell's deviation from the expected relationship may be due to an amplification effect due to the combination of high precipitation and warm temperatures during the same season, or there may be other site-specific factors in Acapulco responsible for the high apparent  $\delta^{18}\text{O}_{\text{sw}}$  value (Section VI).

### V. A synthetic $\delta^{18}\text{O}$ model based on temperature and precipitation

Temperature and precipitation patterns can be either in-phase or out of phase, and the exact relationship varies from environment to environment. This real-world complexity is not taken into account by the simple subtraction method to calculate apparent range in  $\delta^{18}\text{O}_{\text{sw}}$  (Eqns 4 and 5). In order to investigate the constructive and destructive seasonal effects on the range in carbonate  $\delta^{18}\text{O}$  when precipitation and temperature cycles are either in or out of phase, we used the smoothed polynomial temperature and precipitation curves to create a synthetic annual  $\delta^{18}\text{O}$  profile and compare that to the measured range. This was done by scaling the temperature and precipitation models to  $\delta^{18}\text{O}$  units and adding them together.

The temperature curve was scaled by a factor of -0.21, according to the equation for aragonite from Kim et al., 2007 to convert SST to  $\delta^{18}\text{O}$  units. There is no equivalent known scaling factor for precipitation. Additionally, multiple factors could influence the relationship between precipitation and  $\delta^{18}\text{O}_{\text{sw}}$ , including the local geography and average  $\delta^{18}\text{O}_{\text{precip}}$  value at each location, and the appropriate scaling factor could therefore be variable among the different sites. However, since these factors will never be known for paleo sites, we chose to find a single, average scaling factor that could provide an approximate estimate without needing other sorts of information. This factor was calculated through an optimization process, which determined a scale for each shell such that the synthetically generated  $\delta^{18}\text{O}$  (from scaled temperature and precipitation) was equal to the range in  $\delta^{18}\text{O}$  that had been physically observed (described in detail in supplement, figure S5). The optimization gave both a positive and a negative solution,

and the negative solution was selected, since mechanistically, we expect that higher precipitation would lead to lower coastal  $\delta^{18}\text{O}_{\text{sw}}$  values, and therefore lower carbonate  $\delta^{18}\text{O}$  values. The negative solutions for each shell were then averaged, excluding the samples for which the scaling factor was found to be 0, since precipitation did not significantly affect the  $\delta^{18}\text{O}$  range in some cases (shells from England and Puerto Penasco). The resulting mean best scaling factor was  $-1/332$  (see supplement for further details on determining the precipitation scaling factor).

After the temperature and precipitation values were scaled by their respective coefficients, the mean was subtracted in order to center the sinusoid around  $\delta^{18}\text{O} = 0$ . Then, the temperature and precipitation sinusoids were added in order to produce the resulting synthetic  $\delta^{18}\text{O}$  curve. This removes information about the absolute  $\delta^{18}\text{O}$  values that could be achieved in higher or lower precipitation regimes, but is acceptable here because we are focusing on just the range, not the absolute values. The calculation was made as follows:

$$\delta^{18}\text{O}_{\text{month}} = -0.21(\text{SST}_{\text{month}} - \text{SST}_{\text{mean}}) - 1/332 * (\text{PPT}_{\text{month}} - \text{PPT}_{\text{mean}}) \quad (7)$$

Figure 12 shows the resulting synthetic  $\delta^{18}\text{O}$  profiles (black lines), which all contain 12 points tracing out an annual curve. This figure makes it clear what we inferred from Figures 7 and 8 – that certain sites are more strongly influenced by changes in SST (e.g. non-tropical sites) and others by changes in precipitation (e.g. most tropical sites). For example, the synthetic  $\delta^{18}\text{O}$  profile from England closely follows the SST profile, showing that when seasonal variance in precipitation is low and seasonal temperature range is high, precipitation variance will have a minimal effect on the final  $\delta^{18}\text{O}$  range. In contrast, in tropical localities like Colombia, where SST variation is low, the seasonal range in

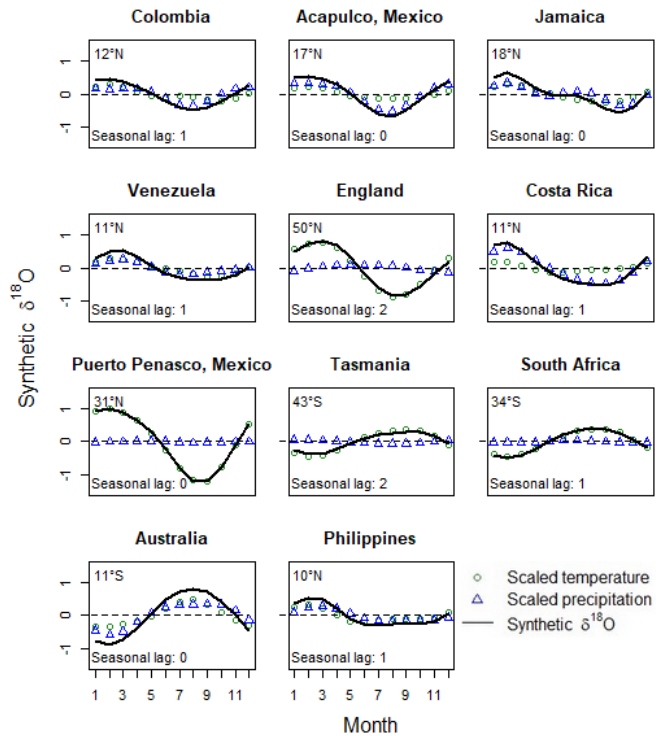


Figure 12: Creation of the synthetic  $\delta^{18}\text{O}$  profiles from modeled subannual temperature and precipitation data, scaled and centered on the x-axis.

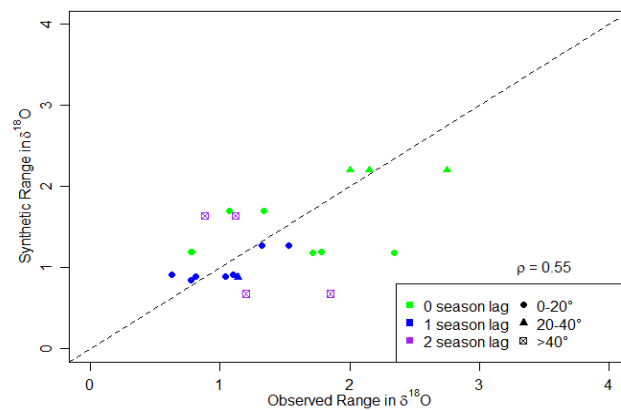


Figure 13: Synthetically generated  $\delta^{18}\text{O}$  ranges plotted against actual observed  $\delta^{18}\text{O}$  ranges. Dashed line is the 1:1 line.

precipitation has a larger influence (seen in the black line following more closely to the blue symbols). Some sites like Tasmania show minor damping effects when the seasonal lag is at a maximum (= 2), where the resulting synthetic  $\delta^{18}\text{O}$  profile is flattened due to the opposing seasonal effects of temperature and precipitation. In contrast, the Australian site shows an amplification effect, where the synthetic  $\delta^{18}\text{O}$  profile has an inflated range due to the superposition of the temperature and precipitation sinusoids.

Figure 13 shows the synthetic ranges plotted against the observed ranges, with a 1:1 line for reference. The residuals away from the 1:1 line range from 0.05 at the minimum to 1.17 at a maximum, with a median value of 0.54. Stated another way, our synthetic profiles recreate the  $\delta^{18}\text{O}$  range within 0.5‰ on average, using a single scaling factor for all sites. The correlation coefficient for the synthetic range and the true, observed range is 0.55. The variation is likely due to other factors like the  $\delta^{18}\text{O}_{\text{precip}}$ , or site-specific geography like rivers, mountains or lakes that may concentrate or change the amount and isotopic composition of freshwater influx to the coast from local precipitation. These local factors were purposefully not taken into account through calculation of a single average scaling factor to make it more applicable to paleoenvironments where these factors are rarely known, so it is expected that there will be some spread in the data.

## VI. Analysis of synthetic data

We compared the behavior of our synthetic data with the real sample data by recreating Figures 7, 8 and 9 using the synthetic  $\delta^{18}\text{O}$  ranges. Figure 14 shows the synthetic range in  $\delta^{18}\text{O}$  vs. the range in SST at each location. For the non-tropical sites, there is a strong correlation between the range in SST and the synthetic range in  $\delta^{18}\text{O}$  (blue dashed line,  $R^2 = 0.98$ ,  $\rho = 0.99$ ), as expected. This is also visible in Figure 12, which show that when precipitation variance is minimal compared to temperature variability, the synthetic profiles strongly follow the SST signal.

Figure 15 shows the synthetic  $\delta^{18}\text{O}$  range plotted against the seasonal precipitation variance. As we saw in our real data (Fig 8), the tropical locations show a strong linear relationship between SPV and  $\delta^{18}\text{O}$  range. Tropical SST range is low (<3°C), meaning  $\delta^{18}\text{O}$  range is primarily influenced by the seasonal precipitation. Higher latitude points fall higher than expected from the tropics-only relationship due to higher seasonal temperature changes increasing the  $\delta^{18}\text{O}$  range. When the SST signal has been removed according to Eqns 4 and 5 in order to calculate the apparent change in  $\delta^{18}\text{O}_{\text{sw}}$ , high latitude points are brought down and into alignment with the linear relationship seen in tropical points (Figure 16). The linear fit through these synthetic points is nearly identical to the relationship found for the real-world points (Eqn 6), and was quantified as follows:

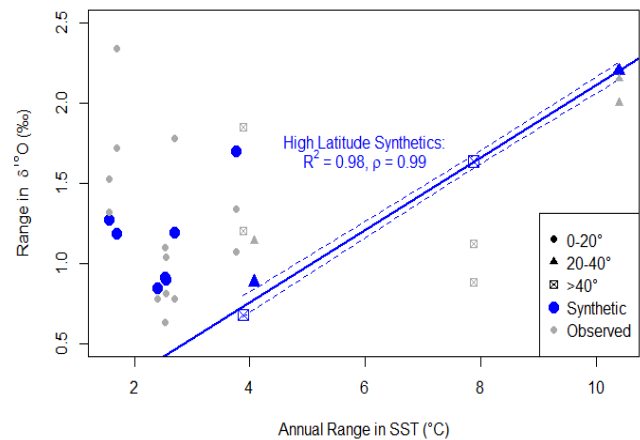


Figure 14: Synthetically generated  $\delta^{18}\text{O}$  ranges (blue) plotted against annual range in SST. Observed ranges in gray for comparison. The correlation is very high for the synthetic non-tropical points (latitude >20°, blue line) but the tropical points have high variance, due to the influence of precipitation.

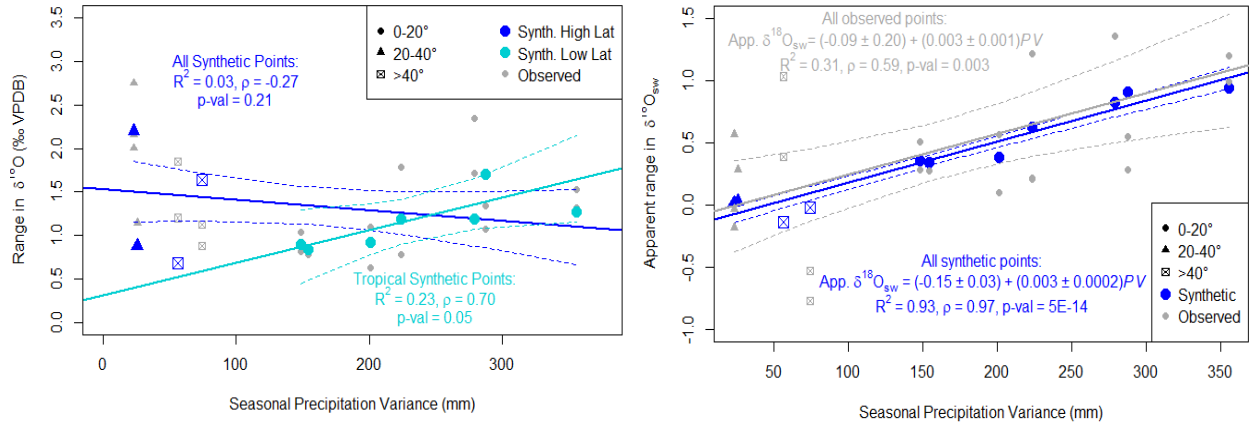


Figure 15 (left). Synthetic  $\delta^{18}\text{O}$  ranges plotted against seasonal precipitation variance. Tropical points show a linear trend, but high-latitude points do not, as seen in the measured data in Figure 8. Figure 16 (right). Synthetic apparent  $\delta^{18}\text{O}_{\text{sw}}$  plotted against precipitation variance. By removing the SST signal, the points are significantly linearized and the linear fit (blue) is nearly identical to the observed data model (gray) in coefficients, but with much stronger correlation due

$$\text{Apparent range in } \delta^{18}\text{O}_{\text{sw}} = (-0.15 \pm 0.03) + (0.003 + 0.0002) * \text{SPV} \quad (8a)$$

$$\text{SPV} = (330 \pm 19) * (\delta^{18}\text{O}_{\text{range}} - 0.21 * \Delta\text{SST}) + (45.4 \pm 11) \quad (8b)$$

This relationship through synthetic data has an  $R^2$  of 0.93 and  $\rho = 0.97$ , far better than the real-world data, which has significant noise. This noise may be due to species-specific vital effects, or potentially due to environmental differences in habitat – a shell living near to the mouth of large river may record a different seasonal  $\delta^{18}\text{O}_{\text{sw}}$  than one living further away from direct riverine input. The specific geography of each site may also influence the  $\delta^{18}\text{O}$  value of both local precipitation and freshwater runoff due to processes such as Rayleigh distillation. If there are mountains near the site, this could plausibly increase the seasonal  $\delta^{18}\text{O}$  range recorded by the shell, as very isotopically light freshwater would have an outsized impact on  $\delta^{18}\text{O}_{\text{sw}}$  when it reaches the coast. This phenomenon may be at play in locations such as Acapulco, Mexico, where the Sierra Madre del Sur mountain range drains into Acapulco Bay via the Papagayo river (Velázquez-Zapata, 2019). The presence of these mountains would lead to very  $^{18}\text{O}$ -depleted rainwater, which could be the reason that both samples from Acapulco recorded higher precipitation variances than actual.

However, despite the noise, the coefficients of the observed relationship are nearly identical to the model found for the synthetic data, providing proof of concept for our apparent range in  $\delta^{18}\text{O}_{\text{sw}}$  calculation method.

## VII. Effects of seasonal lag on $\delta^{18}\text{O}$ range

The calculation of apparent  $\delta^{18}\text{O}_{\text{sw}}$  assumes that the contributions of changing SST and precip are additive and in phase. If the season with maximum precipitation is not the season with maximum temperature (summer), the resulting destructive interference will decrease the observed carbonate  $\delta^{18}\text{O}$  range to varying degrees depending on the lag and the relative magnitudes of SST and precipitation variance. In order to determine the effect of seasonal lag on these relationships, we created six synthetic ‘locations’ by combining temperature regimes from

England (high latitude, high SST range) and Costa Rica (low latitude, low SST range) each with three different precipitation regimes (low, medium, and high precipitation variance) (Table 1). Each synthetic location then had the precipitation profile shifted by 0, 3 and 6 months backwards in order to assess the effect of seasonal lag. Figure 17 shows the resulting synthetic  $\delta^{18}\text{O}$  profiles for these hypothetical sites and Figures 18 and 19 summarize how different seasonal lags affect the carbonate  $\delta^{18}\text{O}$  range, apparent range in  $\delta^{18}\text{O}_{\text{sw}}$ , and estimated temperature range.

Table 1. Creation of the synthetic locations to study the effect of seasonal lag on varying climates.

Synthetic Location	Temperature Regime	Precipitation Regime
(HH) High Lat/High Precip	England, 8°C annual range	Acapulco, 279mm variance
(HM) High Lat/Med Precip	England, 8°C annual range	Venezuela, 148mm variance
(HL) High Lat/Low Precip	England, 8°C annual range	Tasmania, 56mm variance
(LH) Low Lat/High Precip	Costa Rica, 2°C annual range	Acapulco, 279mm variance
(LM) Low Lat/Med Precip	Costa Rica, 2°C annual range	Venezuela, 148mm variance
(LL) Low Lat/Low Precip	Costa Rica, 2°C annual range	Tasmania, 56mm variance

When the seasonal lag is 0 (i.e. maximum precipitation occurs during the summer, top row of Fig 17), the synthetic  $\delta^{18}\text{O}$  range is amplified relative to that expected from temperature alone (green bars show temperature range in  $\delta^{18}\text{O}$  units, black bars show resulting synthetic  $\delta^{18}\text{O}$  range). This is because during periods of increased precipitation, coastal  $\delta^{18}\text{O}_{\text{sw}}$  is driven more negative, leading to more negative  $\delta^{18}\text{O}_{\text{carb}}$ , which appears to represent even warmer temperatures. If workers used the typical method of converting  $\delta^{18}\text{O}_{\text{carb}}$  range straight to SST range, this would result in an overestimation of the paleoseasonality in temperature. In our

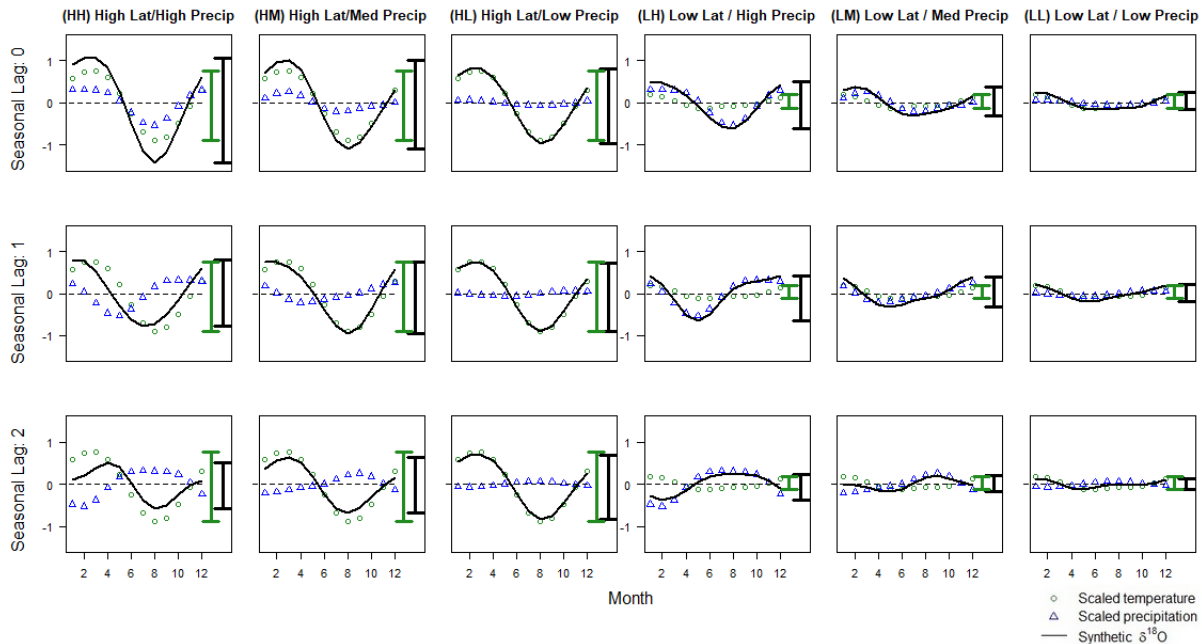


Figure 17: Synthetic  $\delta^{18}\text{O}$  profiles for locations described in Table 1. Green bar shows temperature range scaled into  $\delta^{18}\text{O}$  units. Black bar on side shows resulting synthetic  $\delta^{18}\text{O}$  range for each scenario.

synthetic locations, this can lead to anywhere from 0.5-4°C overestimation of paleoseasonality in low to high precipitation variance regimes (Fig 18, green pts).

As seasonal lag increases to 2 (i.e. highest precipitation occurring during the winter), the destructive interference between the SST and SPV signals increases, leading to a reduction in the modeled  $\delta^{18}\text{O}$  range. If highest precipitation occurs when temperatures are coldest, these effects would compete to reduce/increase  $\delta^{18}\text{O}$  values and result in a muted signal. If workers used the typical method of converting  $\delta^{18}\text{O}_{\text{carb}}$  range straight to SST range, this would result in an underestimation of the paleoseasonality in temperature. In our synthetic locations, when

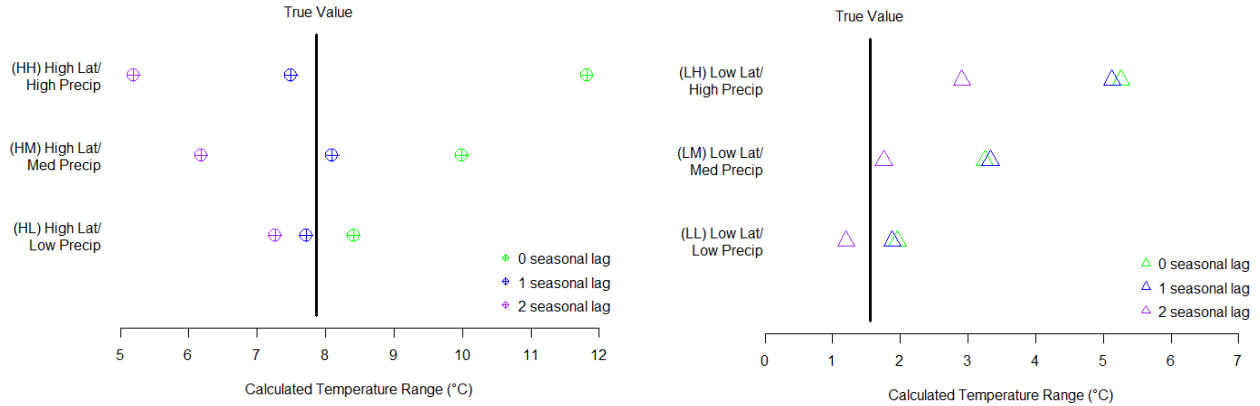


Figure 18: Comparison between calculated temperature range assuming invariant  $\delta^{18}\text{O}_{\text{sw}}$ , and the true temperature range for high latitude (high temperature variance) synthetic sites (a, left) and for low-latitude (low temperature variance) synthetic sites (b, right).

temperature seasonality is high (high latitude sites), a seasonally lag with precipitation can lead to an underestimation of temperature seasonality of 0.5-3°C. In low latitude environments where the SST range is small, this leads to 0.5°C underestimation to 2°C degrees overestimation (Figure 18, purple points).

Treating our synthetic data from the 6 hypothetical locations as real data, we subtract out the SST contribution to  $\delta^{18}\text{O}$  using equations 4 and 5. The resulting apparent range in  $\delta^{18}\text{O}_{\text{sw}}$  is then compared to SPV in figures similar to Figure 9 showing real data. The synthetic data from

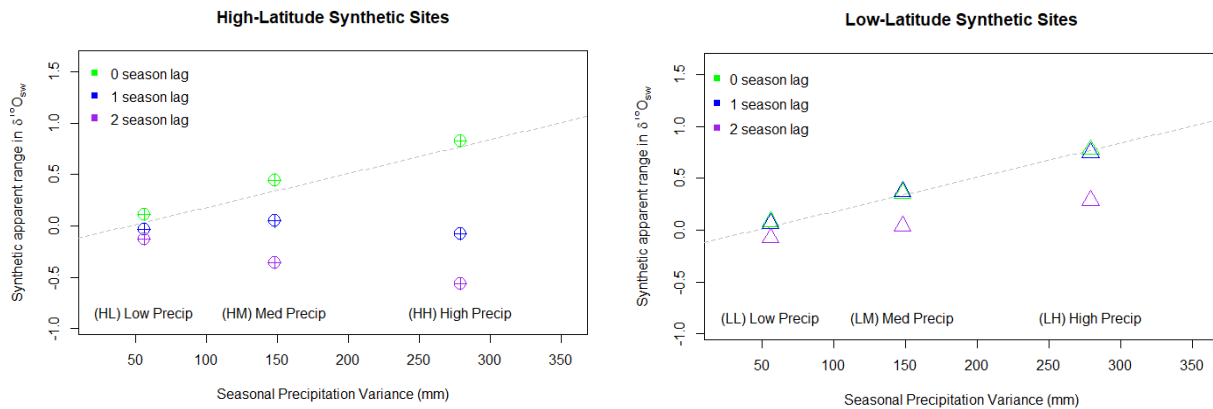


Figure 19: Synthetic locations plotted alongside the apparent  $\delta^{18}\text{O}_{\text{sw}}$  model developed by the synthetic points in Figure 16 (dashed line, eqn 8). 19a (left) shows synthetic locations HH, HM and HL, sites with a high-latitude seasonal temperature range. 19b (right) shows LH, LM and LL, sites with low (tropical) seasonal temperature ranges. Seasonal lag has a stronger effect on high-latitude sites than low-latitude, and is stronger when precipitation is highly seasonal (e.g. HH, LH).

our 6 hypothetical locations generally follow the relationship defined by equation 8. The largest deviations are seen in high latitude sites (high SST range) with medium or high precipitation and 1 or 2 season lag. This is consistent with our real-world data, which shows the largest deviations for high latitude sites with 2 season lag (England, Tasmania).

No previous sclerochronology studies with *Turritella* have taken seasonal lag into account. Figure 18 shows that converting  $\delta^{18}\text{O}$  range to SST range directly (assuming  $\delta^{18}\text{O}_{\text{sw}}$  is constant) has the potential to either over or underestimate SST range. This may not be as much of a problem in real applications as it appears to be in our synthetic hypothetical locations, as it is unlikely there are many real climates with a high precipitation variance (due to monsoonal effects) and a very high temperature range due to the high-latitude location. However, these sorts of effects may still play a role in adding error to reconstructed temperatures.

### **VIII. Potential applications**

The final equation for relating subannual ranges in  $\delta^{18}\text{O}$  with seasonal SST variations and precipitation variance is as follows:

$$SPV = (329 \pm 99) * (\delta^{18}O_{range} - 0.21 * \Delta SST) + (27.4 \pm 61) \text{ (6c, observed data)}$$

$$SPV = (330 \pm 19) * (\delta^{18}O_{range} - 0.21 * \Delta SST) + (45.4 \pm 11) \text{ (8b, synthetic data)}$$

The ability to relate seasonal-scale precipitation patterns with a recorded quantity like  $\delta^{18}\text{O}$  range could open many doors in paleoclimatology. However, this method does not eliminate the problem of relying on the underconstrained  $\delta^{18}\text{O}_{\text{carb}}$  system alone. To use the above equation to estimate SPV in the past, you must have an independent estimate of annual SST range for the site. In a best case scenario, this could be accomplished with another paired proxy, such as clumped isotopes or alkenones. In a less ideal scenario, the SST range could be set as equivalent to today, or could be estimated from a global climate model output. There may be sites where the precipitation regime has changed (thus changing  $\delta^{18}\text{O}_{\text{sw}}$  in coastal areas), but the temperature seasonality has not. Assuming a modern temperature variation in places like these is therefore likely to be a more robust assumption than assuming a modern, seasonally-invariant  $\delta^{18}\text{O}_{\text{sw}}$  value. For example, in the tropics, where annual SST ranges are generally low and invariable through time, assuming a modern SST range is likely a very robust assumption. For example, a qualitative version of this approach was taken by Scholz et al (2020) in the tropical location of Colombia (10°N). The authors assumed that the annual SST range in the Miocene was the same as today (2-3°C). As a result, the much higher  $\delta^{18}\text{O}$  range seen in fossil shells compared to modern ones indicated much higher SPV in the Miocene, argued to be due to a northward migration of the ITCZ. Given this, it is possible that given the right sample collection sites (a latitudinal gradient), this method could be used to track the location of rain belts like the ITCZ, atmospheric rivers, or prevailing storm tracks, all of which are difficult to reconstruct with other geochemical proxies.

### **Conclusion:**

Interpreting the  $\delta^{18}\text{O}$  profiles of shallow coastal organisms like turritellids can be tricky, since they combine signals from multiple climate processes into one record and are susceptible to



local-scale variations. We find that turrnellids are good recorders of relative MASST, though they show an offset of 1.5‰ which we propose is a previously undocumented vital effect. However, on a seasonal scale, it is not adequate to treat  $\delta^{18}\text{O}$  as a direct proxy for seasonal temperature changes, especially in shallow coastal environments that turrnellids inhabit. The subannual range in  $\delta^{18}\text{O}_{\text{carb}}$  recorded in a turrnellid is controlled by both SST range and precipitation variance (controlling  $\delta^{18}\text{O}_{\text{sw}}$  via freshwater discharge). In tropical locations, the range in  $\delta^{18}\text{O}$  is more strongly controlled by seasonal precipitation variance, whereas in high latitudes it is more strongly controlled by temperature variations. This is confirmed through our synthetic data, which follow the precipitation regime closely when temperature seasonality is low, but follow the temperature more closely in high latitude sites with a significant seasonal temperature range. If the contribution of SST range is removed using the known scaling factor from Kim et al, the apparent range in  $\delta^{18}\text{O}_{\text{sw}}$  is highly correlated with precipitation variance, according to the following equation  $SPV = (329 \pm 99) * (\delta^{18}\text{O}_{\text{range}} - 0.21 * \Delta\text{SST}) + (27.4 \pm 61)$ . This calculation of apparent  $\delta^{18}\text{O}_{\text{sw}}$  is a potential new tool to use in paleoclimate reconstructions, assuming that a fairly accurate assessment of the annual range in SST can be made by some other means. This method is likely most robust in tropical sites, where the SST range is low and potentially very similar to modern. Estimating seasonal precipitation variance will allow us to make inferences about past precipitation patterns such as the movement of the ITCZ, Koppen zones, and many other factors which will help us form more fully realized reconstructions of the past.

In addition, we find that a lag between the season of maximum temperature (summer) and precipitation (variable) can lead to either constructive or destructive interference in the resulting  $\delta^{18}\text{O}$  profile, depending on the relative magnitude of the temperature and precipitation ranges. Alignment between maximum temperature and maximum precipitation leads to an overestimation of SST range if  $\delta^{18}\text{O}_{\text{sw}}$  is assumed to be constant. This is not currently taken into account in most sclerochronology studies, but is likely very important in climate regimes like the tropics, where seasonal precipitation is high.

Turrnellids are an under-studied yet extremely widespread genus with a variety of potential paleoclimate applications. Their shallow nearshore habitat means that the isotopic composition of their shell records information about precipitation patterns, unlike deeper-dwelling shells that inhabit waters with more average ocean compositions. However, this coastal habitat also means that they are subject to the influence of many more factors than deep-sea dwelling organisms. The complexity and ambiguity of these records can be frustrating in some ways, as it makes disentangling the multiple signals and variables difficult. However, it also means that this sclerochronological data is rich with multiple types of information about the climate, if we can figure out how to properly extract it.

## References:

- Allmon, W.D., Jones, D.S., and Vaughn, N., 1992, Observations on the biology of *Turritella gonostoma Valenciennes* (Prosobranchia: Turritellidae) from the Gulf of California: *The Veliger*, v. 35, p. 52-63.
- Allmon, W.D., Jones, D.S., Aiello, R.L., Gowlett-Homes, K., and Probert, P.K., 1994, Observations on the biology of *Maoricolpus roseus* (Quoy and Gaimard) (Prosobranchia: Turritellidae) from New Zealand and Tasmania: *The Veliger*, v. 37, p. 267-279.
- Allmon, W.D., 2011, Natural History of Turritelline Gastropods (Cerithioidea: Turritellidae): A Status Report: *Malacologia*, v. 54, p. 159–202, doi:10.4002/040.054.0107.
- Anderson, B.M., and Allmon, W.D., 2020, High calcification rates and inferred metabolic trade-offs in the largest turritellid gastropod, *Turritella abrupta* (Neogene): *Palaeogeography, Palaeoclimatology, Palaeoecology*, v. 544, p. 109623, doi:10.1016/j.palaeo.2020.109623.
- Andreasson, F.P., and Schmitz, B., 2000, Temperature seasonality in the early middle Eocene from  $\delta^{18}\text{O}$  profiles of marine gastropod shells: *GFF*, v. 122, p. 9–10, doi:10.1080/11035890001221009.
- Andreasson, F.P., and Schmitz, B., 1998, Tropical Atlantic seasonal dynamics in the Early Middle Eocene from stable oxygen and carbon isotope profiles of mollusk shells: *Paleoceanography*, v. 13, p. 183–192, doi:10.1029/98PA00120.
- Andreasson, F.P., and Schmitz, B., 1996, Winter and summer temperatures of the early middle Eocene of France from *Turritella*  $\delta^{18}\text{O}$  profiles: *Geology*, v. 24, p. 1067-1070.
- Beck, H.E., Zimmermann, N.E., McVicar, T.R., Vergopolan, N., Berg, A., and Wood, E.F., 2018, Present and future Köppen-Geiger climate classification maps at 1-km resolution: *Scientific Data*, v. 5, p. 180214, doi:10.1038/sdata.2018.214.
- Buick, D.P., and Ivany, L.C., 2004, 100 years in the dark: Extreme longevity of Eocene bivalves from Antarctica: *Geology*, v. 32, p. 921, doi:10.1130/G20796.1.
- Carrillo-Briceño, J.D., Luz, Z., Hendy, A., Kocsis, L., Aguilera, O., and Vennemann, T., 2019, Neogene Caribbean elasmobranchs: Diversity, paleoecology and paleoenvironmental significance of the Cocinetas Basin assemblage (Guajira Peninsula, Colombia): *Biogeosciences*, v. 16, p. 33–56, <https://doi.org/10.5194/bg-16-33-2019>.
- Dettman, D.L., Flessa, K.W., Roopnarine, P.D., Schöne, B.R., and Goodwin, D.H., 2004, The use of oxygen isotope variation in shells of estuarine mollusks as a quantitative record of seasonal and annual Colorado river discharge 1 Associate editor: K. K. Falkner: *Geochimica et Cosmochimica Acta*, v. 68, p. 1253–1263, doi:10.1016/j.gca.2003.09.008.
- Harris, I., Jones, P.D., Osborn, T.J., and Lister, D.H., 2014, Updated high-resolution grids of monthly climatic observations - the CRU TS3.10 Dataset: Updated high-resolution grids of monthly climate observations: *International Journal of Climatology*, v. 34, p. 623–642, doi:10.1002/joc.3711.
- Hendy, A.J.W., Jones, D.S., Moreno, F., Zapata, V., and Jaramillo, C., 2015, Neogene molluscs, shallow marine paleoenvironments, and chronostratigraphy of the Guajira Peninsula, Colombia: *Swiss Journal of Palaeontology*, v. 134, p. 45–75, <https://doi.org/10.1007/s13358-015-0074-1>.

- Huang, B., Thorne, P.W., et. al, 2017, Extended Reconstructed Sea Surface Temperature version 5 (ERSSTv5), Upgrades, validations, and intercomparisons: *J. Climate*, doi: 10.1175/JCLI-D-16-0836.1
- Ivany, L.C., 2012, Reconstructing Paleoseasonality from Accretionary Skeletal Carbonates—Challenges and Opportunities: *The Paleontological Society Papers*, v. 18, p. 133–166, doi:10.1017/S108933260000259X.
- Joetzer, E., Douville, H., Delire, C., and Ciais, P., 2013, Present-day and future Amazonian precipitation in global climate models: CMIP5 versus CMIP3: *Climate Dynamics*, v. 41, p. 2921–2936, doi:10.1007/s00382-012-1644-1.
- Jones, D.S., and Allmon, W.D., 1995, Records of upwelling, seasonality and growth in stable-isotope profiles of Pliocene mollusk shells from Florida: *Lethaia*, v. 28, p. 61–74, doi:10.1111/j.1502-3931.1995.tb01593.x.
- Kim, S.-T., O’Neil, J.R., Hillaire-Marcel, C., and Mucci, A., 2007, Oxygen isotope fractionation between synthetic aragonite and water: Influence of temperature and Mg<sup>2+</sup> concentration: *Geochimica et Cosmochimica Acta*, v. 71, p. 4704–4715, doi:10.1016/j.gca.2007.04.019.
- LeGrande, A.N., and Schmidt, G.A., 2006, Global gridded data set of the oxygen isotopic composition in seawater: *Geophysical Research Letters*, v. 33, p. L12604, doi:10.1029/2006GL026011.
- Moreno, F., et al., 2015, Revised stratigraphy of Neogene strata in the Cocinetas Basin, La Guajira, Colombia: *Swiss Journal of Palaeontology*, v. 134, p. 5–43, doi: <https://doi.org/10.1007/s13358-015-0071-4>.
- Scholz, S.R. et al., 2020, Isotope sclerochronology indicates enhanced seasonal precipitation in northern South America (Colombia) during the Mid-Miocene Climatic Optimum: *Geology*, doi:10.1130/G47235.1.
- Schmidt, G.A., Bigg, G.R., and Rohling, E.J, 1999, Global Seawater Oxygen-18 Database v1.22, <https://data.giss.nasa.gov/o18data/>
- Steuber, T., 1996, Stable isotope sclerochronology of rudist bivalves: Growth rates and Late Cretaceous seasonality: *Geology*, v. 24, p. 315-318.
- Surge, D., Lohmann, K.C., and Dettman, D.L., 2001, Controls on isotopic chemistry of the American oyster, *Crassostrea virginica* : implications for growth patterns: *Palaeogeography, Palaeoclimatology, Palaeoecology*, v. 172, p. 283–296, doi:10.1016/S0031-0182(01)00303-0.
- Tao, K., Robbins, J.A., Grossman, E.L., and O’Dea, A., 2013, Quantifying Upwelling and Freshening in Nearshore Tropical American Environments Using Stable Isotopes in Modern Gastropods: *Bulletin of Marine Science*, v. 89, p. 815–835, doi:10.5343/bms.2012.1065.
- Velázquez-Zapata, J.A., 2019, Comparing Meteorological Data Sets in the Evaluation of Climate Change Impact on Hydrological Indicators: A Case Study on a Mexican Basin: *Water*, v. 11, p. 2110, doi:10.3390/w11102110.

## Chapter 2: Supplemental Information

Table S1. Rectangular regions ( $2^\circ \times 2^\circ$ ) around sample area used to calculate monthly sea surface temperature and precipitation values. Average values were latitude-weighted to correct for changes in grid size area with latitude.

<b>Location</b>	<b>Longitude Range</b>	<b>Latitude Range</b>
Acapulco, Mexico	98-100°W	16-18°N
Colombia	70-72°W	11-13°N
Costa Rica	84-86°W	10-12°N
England	4-6°W	49-51°N
Jamaica	76.5-78.5°W	17-19°N
Philippines	123-125°E	9-11°N
Puerto Penasco, Mexico	112-114°W	30-32°N
South Africa	24-26°E	33-35°S
Tasmania	146-148°E	42-44°S
Venezuela	62-64°W	9-11°N

Figure S1. Correlation between  $\delta^{18}\text{O}$  and  $\delta^{13}\text{C}$  for all shells. Dashed line is the best fit linear model.

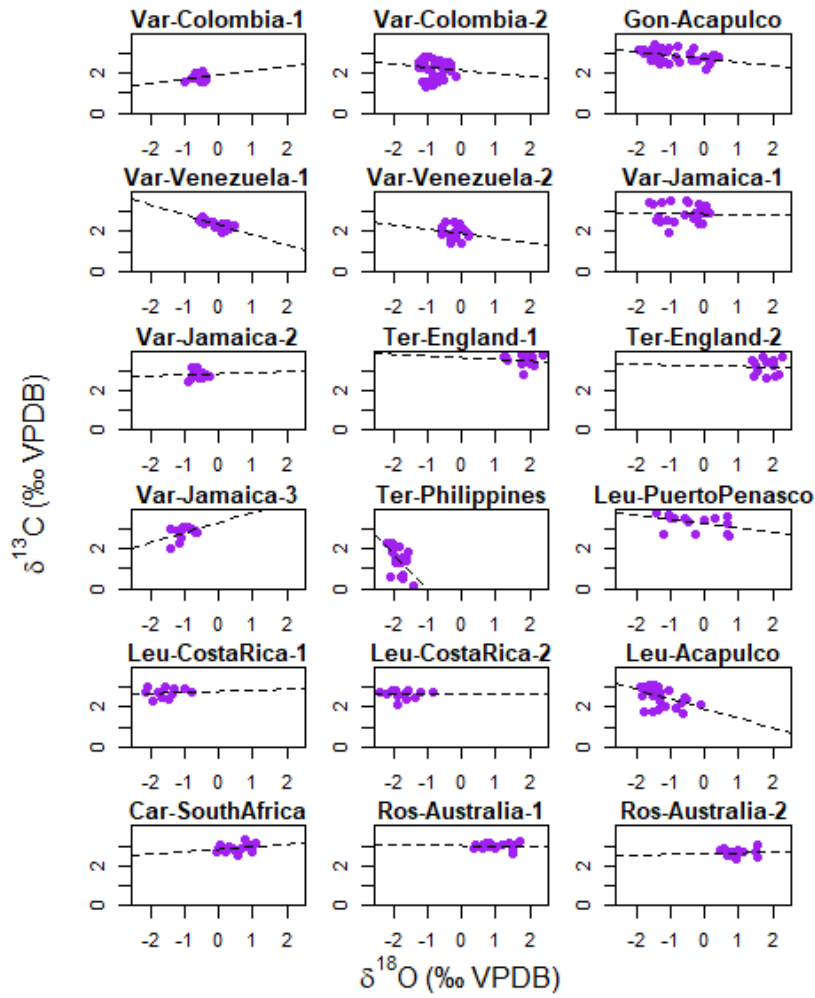


Figure S2. Analysis of relationship between MASST and mean  $\delta^{18}\text{O}$ . Similar relationship was seen to that that shown with median  $\delta^{18}\text{O}$ , no significant difference was found between using the mean and using the median.

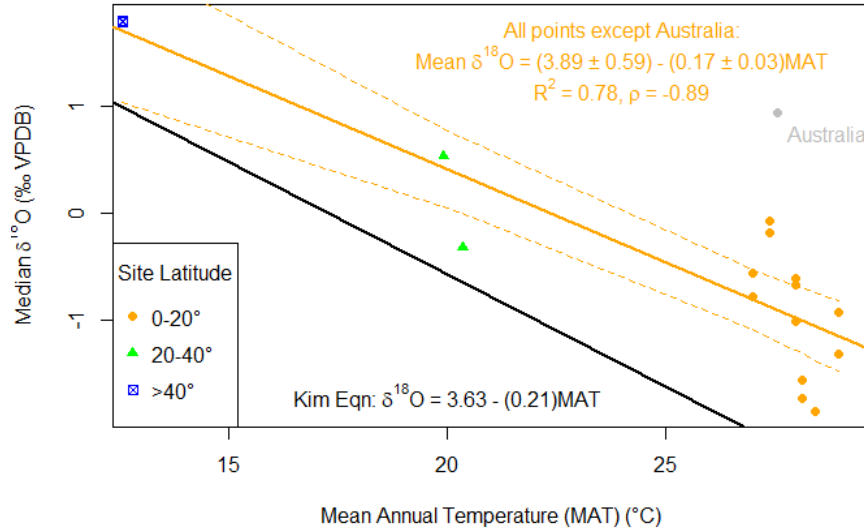
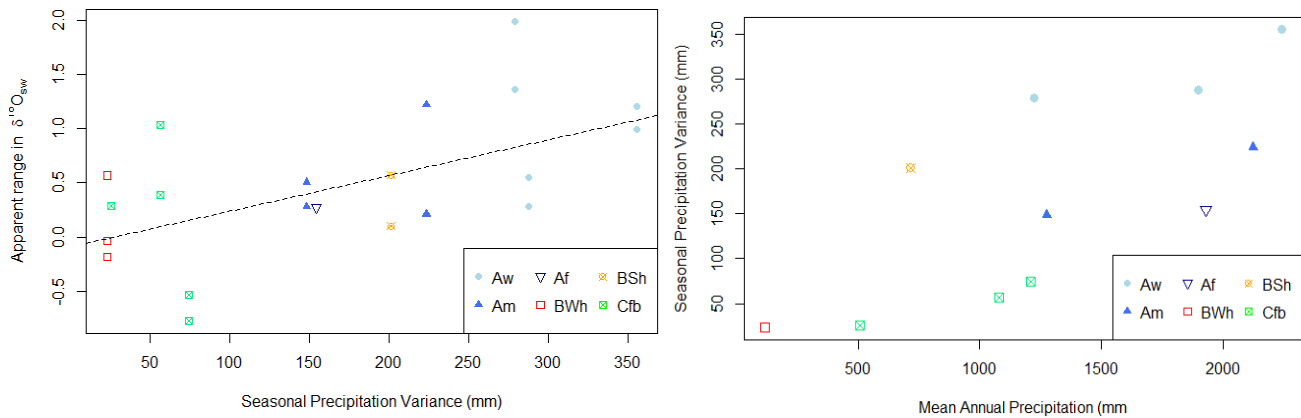


Figure S3. Points colored by their Koppen climate zone classification (according to the maps presented in Beck et al., 2018), along with the linear model. Towards the higher end of precipitation variance and range in apparent  $\delta^{18}\text{O}_{\text{sw}}$ , Aw (tropical savannah, dry winter) climate types dominate. Moving left and down leads into Am and Af climates (tropical monsoonal and tropical rainforest types), and eventually points with low precipitation variance are either Cfb (temperate oceanic) or BWh (hot arid desert) climates. Figure S1b shows seasonal precipitation variance plotted against MAP, in order to show where each of these climate types plot in precipitation-space. Tropical savannah climates are the most seasonally variable, due to their pronounced wet and dry seasons, whereas hot arid deserts plot at the bottom left, with very low MAP and no seasonal variance.



S1a (left): Points colored by Koppen climate classification. Aw = tropical savannah with dry winter; Am = tropical monsoonal; Af = tropical rainforest; BWh = hot arid desert; BSh = hot semi-arid; Cfb = temperate oceanic. S1b (right): Seasonal precipitation variance plotted against MAP for all locations, illustrating the position of each Koppen climate zone.

Figure S4:

Range in  $\delta^{18}\text{O}$  plotted against mean annual precipitation (MAP) for all sites. There is a weak negative correlation, with locations with high MAPs having lower  $\delta^{18}\text{O}$  ranges. This may be due the fact that sites with the highest MAPs are in the tropics, which will be less seasonally variable in temperature than higher latitudes – though the tropical points are variable, as they may still be influenced by seasonal precipitation.

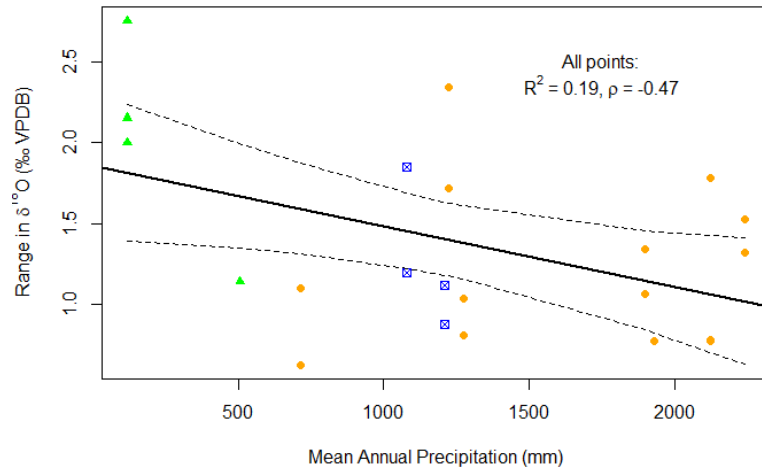




Figure S5: Precipitation scaling factors.

Plots show calculations of the optimum precipitation scaling factors to match the observed  $\delta^{18}\text{O}$  range in each shell. Possible scaling factors included the inverse all integers between -1000 and 1000. For each potential scaling factor, the temperature profile for the location was scaled by 0.21, and the precipitation was scaled by the test factor. A synthetic  $\delta^{18}\text{O}$  range was generated by adding the scaled temperature and precipitation profiles together and finding the minimum and maximum synthetic  $\delta^{18}\text{O}$  values. This synthetic  $\delta^{18}\text{O}$  range was then compared to the observed  $\delta^{18}\text{O}$  range seen in the shell, the difference was recorded as the offset (y-axis). Red dots show where the offset equals zero, i.e. the best scaling factor to match the observed range for a certain shell. There is a positive and a negative solution for each site – the negative was chosen because precipitation will impact  $\delta^{18}\text{O}$  negatively (more precipitation = lower  $\delta^{18}\text{O}$ ). Locations where the precipitation did not play a role in  $\delta^{18}\text{O}$  range due to high SST variance showed asymptotic behavior, where the best scaling factor was the lowest (1/1000). These were removed from the calculation of the mean best scaling factor, as they were not representative of the true precipitation to  $\delta^{18}\text{O}$  range scaling.

